



Contents lists available at SciVerse ScienceDirect

# Earth and Planetary Science Letters

journal homepage: [www.elsevier.com/locate/epslet](http://www.elsevier.com/locate/epslet)



## Pothole and channel system formation in the McMurdo Dry Valleys of Antarctica: New insights from cosmogenic nuclides

Jennifer L. Middleton\*, Robert P. Ackert Jr., Sujoy Mukhopadhyay

Department of Earth and Planetary Sciences, Harvard University, 20 Oxford Street, Cambridge, MA 02138, USA

### ARTICLE INFO

#### Article history:

Received 15 December 2011

Received in revised form

12 August 2012

Accepted 15 August 2012

Editor: J. Lynch-Stieglitz

Available online 30 October 2012

#### Keywords:

cosmogenic nuclide

neon-21

beryllium-10

Antarctica

Dry Valleys

channels

### ABSTRACT

Large pothole and channel features (~15 m deep, ~30 m wide) carved into the Beacon Sandstone in the upland Dry Valleys of Antarctica have been used to infer catastrophic subglacial flooding beneath an expanded East Antarctic Ice Sheet that overran the Transantarctic Mountains during the mid-Miocene. Though the age and erosion rates of these geomorphic features have not been quantified, preservation of the potholes and channels has been attributed to negligible erosion under consistent polar desert conditions since the retreat of the ice sheet at ~14 Ma. We present cosmogenic  $^{21}\text{Ne}$  and  $^{10}\text{Be}$  data from samples collected along vertical transects of pothole and channel walls, as well as from intervening benches, within Battleship Promontory in the Convoy Range and within Sessrummir Valley in the Western Asgard Range to constrain their exposure history. Measurements of fissionogenic  $^{136}\text{Xe}$  are used to estimate a nucleogenic  $^{21}\text{Ne}$  concentration in the Beacon Sandstone of  $7.7 \pm 2.4 \times 10^6 \text{ atoms g}^{-1}$  and to correct our  $^{21}\text{Ne}$  data for this component. Sample concentrations of cosmogenic  $^{21}\text{Ne}$  and  $^{10}\text{Be}$  are significantly lower than previously measured in the regional bedrock and reveal steady state erosion rates ranging from 99 to  $171 \text{ cm Ma}^{-1}$  in Battleship Promontory and from 59 to  $383 \text{ cm Ma}^{-1}$  in Sessrummir Valley. Continuous exposure at such erosion rates would remove 8–54 m of bedrock over a 14 Ma period, a length scale similar to the features themselves, and suggests that these systems could have formed primarily through subaerial erosive processes. Alternatively, if the features formed subglacially in the Miocene, then a complex erosion and exposure history must have occurred to prevent the accumulation of cosmogenic nuclides to levels higher than those observed. Either prolonged and extensive ice cover of these features prior to 2 Ma, or a threefold increase in erosion rates during the Plio-Pleistocene could produce the  $^{21}\text{Ne}$  and  $^{10}\text{Be}$  concentrations measured here. Ultimately, all of these scenarios imply that the upland Dry Valleys landscape has experienced greater changes over the last 14 Ma than previously considered.

© 2012 Elsevier B.V. All rights reserved.

## 1. Introduction

An accurate understanding of the history of the East Antarctic Ice Sheet (EAIS) guides our ability to model the ice sheet's response to future climate trends. The warmer than modern temperatures of the mid-Pliocene (~3 Ma) can provide a climatic analogue to a world heated by anthropogenic emissions of greenhouse gasses (Dowsett et al., 1996; Ravelo et al., 2004). However, the nature of the EAIS during the Pliocene warm period is still debated. Geologic evidence of previous glaciations extending back millions of years in the ice free landscape of the McMurdo Dry Valleys in Antarctica (Fig. 1) makes the region an important resource in reconstructing the history of the EAIS. Cosmogenic nuclide analyses of the Dry Valleys landscape provide constraints on both the ages of these glacially derived geomorphic features

and on their erosion rates (e.g., Margerison et al., 2005; Niedermann, 2002; Schäfer et al., 1999; Summerfield et al., 1999).

Preservation of *in situ* unweathered Miocene ash deposits and the current cold, arid conditions of the uplands between the major trunk valleys of the Dry Valleys have led to the idea that the region has been a polar desert experiencing very little erosion for the past ~14 Ma (Marchant et al., 1993a). Cosmogenic nuclide analyses of granite, dolerite, and sandstone samples from multiple sites within the Dry Valleys support the consistent polar desert hypothesis and indicate regional erosion rates as low as  $10\text{--}30 \text{ cm Ma}^{-1}$  (Brown et al., 1991; Nishiizumi et al., 1991; Schäfer et al., 1999; Summerfield et al., 1999). Following the interpretation that the upland valleys have experienced little alteration over the past 14 Ma and appear to lack younger glacial deposits, it has been argued that neither the EAIS, nor local alpine glaciers, have significantly advanced or retreated since the mid-Miocene despite significant global changes during the Pliocene warm period (Denton et al., 1993; Marchant and Denton, 1996; Marchant et al., 1993a, 1993b; Sugden and Denton, 2004).

\* Corresponding author. Tel.: +1 617 384 9335; fax: +1 617 495 8839.  
E-mail address: jmiddlet@fas.harvard.edu (J.L. Middleton).

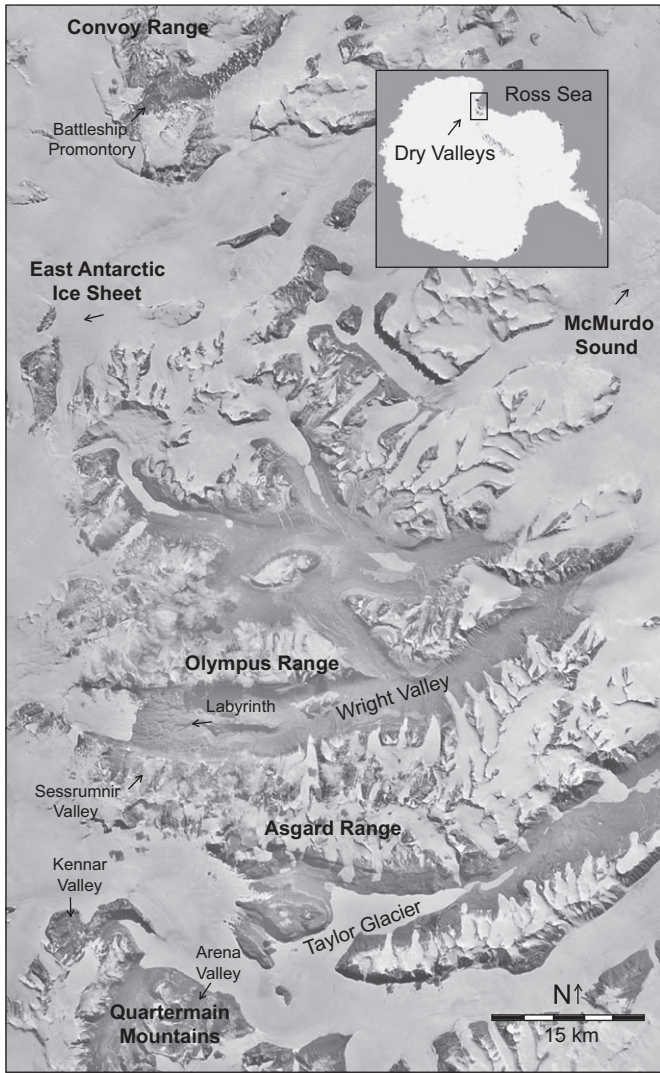


**Fig. 1.** Satellite image of the McMurdo Dry Valleys of Antarctica showing the location of Battleship Promontory, Sessrumnir Valley, and other regions mentioned in the text.

The geomorphology of the Dry Valleys' uplands includes dramatic channel systems ~15 m deep marked with potholes up to ~30 m in diameter carved into the Beacon Sandstone in the Quartermain Mountains, the Asgard Range, and the Convoy Range (Denton et al., 1984; Sugden et al., 1991; Fig. 1). An additional dolerite channel system, known as the Labyrinth, is found in Wright Valley at the terminus of an EAIS outlet glacier (Fig. 1).  $^{40}\text{Ar}/^{39}\text{Ar}$  dating of ash beds and ash-rich diamictites suggests that the Labyrinth was formed between 12.4 and 14.4 Ma (Lewis et al., 2006). The ages of the sandstone pothole and channel systems have not been directly dated, but the formation of both the sandstone features and the Labyrinth is typically attributed to catastrophic subglacial flooding at ~14 Ma during a major expansion of the EAIS over the Transantarctic Mountains and into the Dry Valleys (Denton et al., 1984; Denton and Sugden, 2005; Lewis et al., 2006; Sugden and Denton, 2004).

However, subglacial flooding is not the only mechanism capable of producing channel systems such as those of the Dry Valleys. Subaerial flooding is credited with the formation of the Channeled Scabland in North America, which shares many geomorphic similarities with the Labyrinth and is much larger in scale (Benito and O'Connor, 2003; Bretz, 1969). Alternatively, the combination of salt weathering and strong valley winds has been

proposed as a factor in carving both the dolerite channels of the Labyrinth and the sandstone potholes of the uplands (Selby and Wilson, 1971; Shaw and Healy, 1977). Nonetheless, subglacial production of the potholes and channels during the Miocene is widely accepted and these features have been used as evidence that the landscape of the Dry Valleys' uplands has not changed significantly during the past 14 Ma.

Thus the two linked hypotheses regarding the sandstone potholes and channels of the Dry Valleys are summarized as follows: (1) these features were formed at ~14 Ma by subglacial floods beneath a much larger EAIS and (2) these features have been preserved due to low erosion rates in an unchanging polar desert climate since their formation. Here we present cosmogenic  $^{21}\text{Ne}$  and  $^{10}\text{Be}$  data from three sandstone pothole transects within the Dry Valleys. Analyses of our data suggest that the two hypotheses listed above cannot both be true.

## 2. Sampling and methods

Seventeen bedrock samples of potholes and channels were obtained from Sessrumnir Valley in the Asgard Range and from Battleship Promontory, located ~75 km to the north in the Convoy Range (Fig. 1). Sandstone samples, belonging to the Beacon Supergroup, were taken from benches within the channel systems, from channel floors, and from vertical transects in two potholes in Sessrumnir Valley (Figs. 2 and 3) and in one pothole in Battleship Promontory (Fig. 3). The vertical transects span 10–15 m in height and were made to gather a representative number of samples for investigating the rate of pothole widening from horizontal wall retreat in addition to the deepening rate of the features by vertical erosion. Pits and overhangs along the pothole and channel walls were avoided while collecting vertical transect samples. Topographic shielding measurements of both azimuthal and inclination angles of obstructions were taken for each bench and floor sample and at the base of each transect. Images of each sample, including field photographs of samples not observed in Fig. 3, are presented in Supplementary Fig. S1.

### 2.1. Cosmogenic nuclide calculations

The measurement of both stable and radioactive cosmogenic nuclides is required to constrain the long term (>3 Ma) exposure history of a sample. The production of cosmogenic nuclides in a sample is depth dependent and occurs through spallation, negative

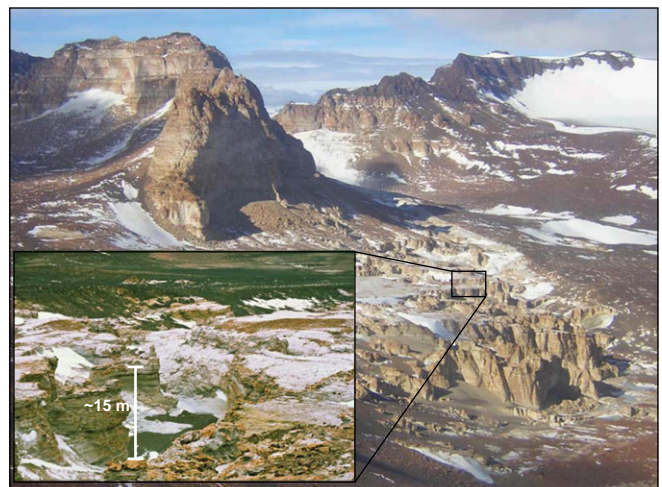


**Fig. 2.** Channel systems in Sessrumnir Valley along with a close-up of typical channel morphology.

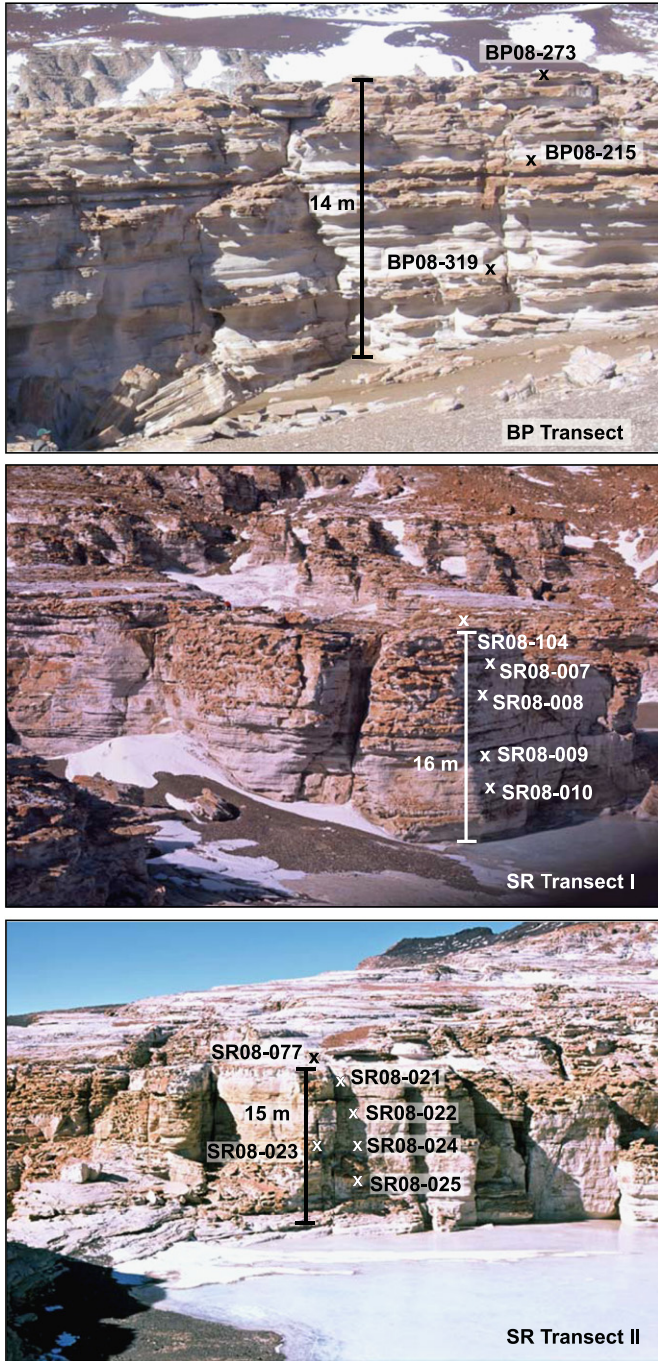


**Fig. 3.** Field photos of transect samples in Battleship Promontory (upper panel) and Sessrummir Valley (lower panels). X's mark the sample locations. Additional sample images are available in Supplementary Fig. S1.

muon capture, and fast muon interactions (Gosse and Phillips, 2001). Losses are caused by erosive processes at the surface and by radioactive decay. Thus, the concentration of a radioactive cosmogenic nuclide  $N(z,t)$  within a sample at depth  $z$  and time  $t$  is given by

$$\begin{aligned}
 N(z,t) = & N(z,0)e^{-\lambda t} + \frac{P_{sp}}{\lambda + \frac{\varepsilon}{\Lambda_{sp}}} \left( e^{\frac{-z}{\Lambda_{sp}}} \right) \left( 1 - e^{-\left( \lambda + \frac{\varepsilon}{\Lambda_{sp}} \right)t} \right) \\
 & + \frac{P_{mu-}}{\lambda + \frac{\varepsilon}{\Lambda_{mu-}}} \left( e^{\frac{-z}{\Lambda_{mu-}}} \right) \left( 1 - e^{-\left( \lambda + \frac{\varepsilon}{\Lambda_{mu-}} \right)t} \right) \\
 & + \frac{P_{mufast}}{\lambda + \frac{\varepsilon}{\Lambda_{mufast}}} \left( e^{\frac{-z}{\Lambda_{mufast}}} \right) \left( 1 - e^{-\left( \lambda + \frac{\varepsilon}{\Lambda_{mufast}} \right)t} \right)
 \end{aligned} \quad (1)$$

where  $N(z,0)$  is the initial nuclide concentration ( $\text{atoms g}^{-1}$ ),  $\lambda$  is the nuclide decay constant ( $\text{yr}^{-1}$ ),  $\varepsilon$  is the erosion rate ( $\text{g cm}^{-2} \text{yr}^{-1}$ ), and  $P_{sp}$ ,  $P_{mu-}$ ,  $P_{mufast}$  and  $\Lambda_{sp}$ ,  $\Lambda_{mu-}$ ,  $\Lambda_{mufast}$  are location-specific surface production rates ( $\text{atoms g}^{-1} \text{yr}^{-1}$ ) and effective attenuation lengths ( $\text{g cm}^{-2}$ ) via spallation, negative muon capture, and fast muon interactions, respectively (Gosse and Phillips, 2001; Lal, 1991). The same equation applies to a stable cosmogenic nuclide where  $\lambda$  is equal to zero. Under ideal analytical conditions, in which production rates are well known and the sample has experienced continuous exposure at a constant erosion rate, defined as simple exposure, the measurement of two cosmogenic nuclides yields both the erosion rate and the exposure age (Gosse and Phillips, 2001; Lal, 1991). If a sample has reached steady state, in which the production of cosmogenic nuclides equals the losses through erosion and radioactive decay, then the calculated time  $t$  is a minimum exposure age for the sample.

In this study, we use a sea level, high latitude, spallation production rate for cosmogenic  $^{10}\text{Be}$  of  $4.49 \pm 0.39 \text{ atom g}^{-1} \text{yr}^{-1}$  (normalized to the 07KNSTD Be standard; Nishiizumi et al., 2007) and include a  $^{10}\text{Be}$  muon induced production rate of  $0.18 \text{ atom g}^{-1} \text{yr}^{-1}$  such that 3.8% of the total  $^{10}\text{Be}$  production rate is attributed to muon related reactions (Balco et al., 2008; Balco and Shuster, 2009). The production rates of cosmogenic  $^{21}\text{Ne}$  (henceforth  $^{21}\text{Ne}_c$  to distinguish from other sample components of  $^{21}\text{Ne}$ ) for spallation and muon interactions are determined using a total  $^{21}\text{Ne}/^{10}\text{Be}$  production ratio of  $4.08 \pm 0.37$  and allowing for 3.6% of the total production rate to stem from muon interactions (Balco and Shuster, 2009). We use  $150 \text{ g cm}^{-2}$ ,  $1510 \text{ g cm}^{-2}$ , and  $4320 \text{ g cm}^{-2}$ , for  $\Lambda_{sp}$ ,  $\Lambda_{mu-}$ , and  $\Lambda_{mufast}$ , respectively (Balco and Shuster, 2009; Heisinger et al., 2002a,b),  $4.994 \times 10^{-7} \text{ yr}^{-1}$  for  $\lambda^{10}\text{Be}$  (Korschinek et al., 2010), and we measure and use a sample density of  $2.5 \text{ g cm}^{-3}$ .

Steady state erosion rates are calculated from concentrations of  $^{21}\text{Ne}_c$  and  $^{10}\text{Be}$  using Stone's (2000) production rate scaling, and follow the equations of Lal (1991) as modified by Balco and Shuster (2009) to account for muon induced production. Corrections for topographic shielding and variations in effective attenuation length due to slope angles of  $75^\circ$  and  $80^\circ$  for the transect sample surfaces are made following the methods of Dunne et al. (1999). We assume that 100% of the muon induced production of  $^{21}\text{Ne}_c$  stems from fast muon interactions, as nuclear systematics suggest that the production of  $^{21}\text{Ne}_c$  from negative muon capture is negligible (Goethals et al., 2009). We use the assumption of fast muon interactions as the dominant muon production source during  $^{10}\text{Be}$  production as well and note that the relative proportions of negative muon capture to fast muon interactions do not affect our conclusions. If, instead, 100% of the muon induced production is attributed to negative muon capture reactions, then the steady state erosion rates calculated from our cosmogenic  $^{10}\text{Be}$  data decrease by  $< 5\%$  from our original estimates.

## 2.2. Measurement of $^{10}\text{Be}$ and $^{21}\text{Ne}$

Techniques for the extraction of  $^{10}\text{Be}$  from quartz and its measurement by AMS are well established. Beryllium samples were prepared at the University of New Hampshire following methods of Licciardi (2000) slightly modified by Goehring (2006). AMS measurements were carried out at PRIME Lab AMS facility at Purdue University and are referenced to the 07KNSTD isotope ratio standard (Nishiizumi et al., 2007). All  $^{10}\text{Be}$  atoms in the quartz samples are attributed to cosmogenic origin.

Neon sample preparations and measurements were conducted at the Noble Gas Laboratory at Harvard University. Samples were coarsely crushed and whole quartz grains without visible impurities or inclusions were manually picked from 0.5 to 1.0 mm grain sized fraction under a binocular microscope. Selected grains

were then leached with ~1.5 ml of a 50% HF solution in a 3:1 mixture with HNO<sub>3</sub> to remove ~40 µm from the outer rind of each grain to eliminate nucleogenic <sup>21</sup>Ne produced from implantation of alpha particles into the quartz crystal. Samples remained in the acid solution for at least 24 h and were ultrasonically shaken periodically to ensure effective leaching of all sample grains. Leached grains were thoroughly rinsed and flushed with distilled water to remove all traces of HF. Samples were examined under a microscope a second time to remove any grains with inclusions revealed by the leaching process and then loaded into Nb packets. Neon measurements were replicated in a subset of the samples. For these repeated samples, excess purified quartz from the Be preparation procedure was crushed and the inclusion bearing grains were removed from 30 to 200 µm sized fraction before loading into Nb packets. Preparations yielded sample masses ranging from 70 to 250 mg.

Each sample was step heated in a furnace from either 410 °C or 750 °C to 1550 °C to release gases trapped within the crystal lattice of the quartz grains. Thermocouple readings, distanced from the hottest part of the furnace, were collected for each heat step. Pyrometer calibrations of furnace temperatures within an empty crucible indicated that for thermocouple readings of 700 °C, 900 °C, and 1250 °C, temperatures of the furnace hot spot where samples bake were 750 °C, 1120 °C, and 1550 °C, respectively. All reported step heating temperatures reflect the furnace hot spot as determined by the pyrometer-thermocouple calibrations. Each 1550 °C step was followed by a repeat extraction step at the same temperature. The repeat gas extraction steps resulted in Ne levels within the range of furnace blank values and demonstrated quantitative extraction of Ne during the step heating.

The evolved gas from each heating step was let into the purification line where reactive components were removed using two SAES Zr-Al alloy getters, one at 450 °C and one at room temperature. Neon and the heavier noble gases were then trapped onto a cryogenic cold-finger at 32 K, allowing for complete separation from evolved He. After He was pumped away, the cold-finger was heated to 74 K to liberate Ne, which was then inlet to the mass spectrometer.

Concentrations of <sup>20</sup>Ne, <sup>21</sup>Ne, and <sup>22</sup>Ne were measured using a Nu Noblesse mass spectrometer operating in multi-collection mode with three discrete dynode multipliers. Background levels of <sup>40</sup>Ar and CO<sub>2</sub> were also measured to correct for doubly charged isobaric interferences on <sup>20</sup>Ne and <sup>22</sup>Ne, respectively. A liquid nitrogen cold trap within the mass spectrometer volume kept Ar and CO<sub>2</sub> backgrounds low. The <sup>40</sup>Ar<sup>2+</sup>/<sup>40</sup>Ar<sup>+</sup> ratio and the CO<sub>2</sub><sup>2+</sup>/CO<sub>2</sub><sup>+</sup> ratio were 0.031 ± 0.003 and 0.0045 ± 0.0005, respectively. For the replicate measurements, the <sup>40</sup>Ar<sup>2+</sup>/<sup>40</sup>Ar<sup>+</sup> ratio and the CO<sub>2</sub><sup>2+</sup>/CO<sub>2</sub><sup>+</sup> ratio were 0.078 ± 0.003 and 0.0079 ± 0.0006. Typical Ne blanks in the 750 °C, 1120 °C, and 1550 °C temperature steps were 9.58, 10.8, and 23.3 × 10<sup>6</sup> atoms of <sup>20</sup>Ne, respectively, and were atmospheric in composition. The <sup>20</sup>Ne concentrations and <sup>22</sup>Ne/<sup>20</sup>Ne and <sup>21</sup>Ne/<sup>20</sup>Ne ratios for the heating steps of each sample are listed in Supplementary Table S1.

### 2.3. Using fissionogenic <sup>136</sup>Xe to correct for nucleogenic <sup>21</sup>Ne

Most of the observed Ne isotopic compositions released in step heating do not fall on a two component mixing line between atmospheric Ne and cosmogenic Ne (Supplementary Fig. S3). Thus, we assume that the <sup>21</sup>Ne in the samples is a three component mixture of atmospheric <sup>21</sup>Ne, cosmogenic <sup>21</sup>Ne<sub>c</sub>, and nucleogenic <sup>21</sup>Ne. Nucleogenic <sup>21</sup>Ne is primarily produced in quartz by <sup>18</sup>O(α,n)<sup>21</sup>Ne reactions. Since at least the outer 40 µm of the quartz samples have been removed by leaching in HF, nucleogenic <sup>21</sup>Ne produced by alpha implantation into the quartz from U and Th residing outside the quartz crystal lattice is

negligible. Hence, the observed nucleogenic Ne likely results from U and Th residing in fluid and mineral inclusions within the analyzed quartz.

As a certain fraction of U decays are spontaneous fission, resulting in the production of <sup>136</sup>Xe, a ratio of nucleogenic <sup>21</sup>Ne to fissionogenic <sup>136</sup>Xe can be calculated based on the Th/U ratio (Ballentine and Burnard, 2002). To constrain the magnitude of our nucleogenic <sup>21</sup>Ne components, we conducted replicate analyses of a subset of our samples to measure both Ne and Xe in the same sample aliquots, similar to the method of Fujioka et al. (2005). The step heating and gas processing protocols for these samples are the same as described above, except that after mass spectrometric measurement of Ne at each temperature step, the cryogenic cold-finger was warmed to release Ar and Kr, which were then pumped away. The cold-finger was subsequently warmed to 340 K to release Xe, which was then inlet into the mass spectrometer. The evolved <sup>130</sup>Xe and <sup>136</sup>Xe were measured simultaneously, followed by peak jumping to <sup>129</sup>Xe. Typical Xe blanks in the 750 °C, 1120 °C, and 1550 °C temperature steps were 1.5, 2.3, and 4.3 × 10<sup>5</sup> atoms of <sup>129</sup>Xe, respectively, and were atmospheric in composition. Quantitative Xe extraction is ensured for each sample by running an additional high temperature step at 1550 °C after the completion of standard step heating. In each case, the Xe levels released during repeat extraction were within the range of our furnace blanks.

Measured <sup>129</sup>Xe/<sup>130</sup>Xe ratios were atmospheric within error and thus, fissionogenic <sup>136</sup>Xe was calculated from the relation:

$$\text{Xe}_{\text{fissionogenic}} = \frac{\text{Xe}_{\text{measured}}}{\left[ \left( \frac{\text{Xe}_{\text{measured}}}{\text{Xe}_{\text{air}}} \right)_{\text{measured}} - \left( \frac{\text{Xe}_{\text{measured}}}{\text{Xe}_{\text{air}}} \right)_{\text{air}} \right]} \quad (2)$$

Total nucleogenic <sup>21</sup>Ne was then calculated for each of the replicate samples using the sum of fissionogenic <sup>136</sup>Xe released from each heat step, and a <sup>21</sup>Ne<sub>nucleogenic</sub>/<sup>136</sup>Xe<sub>fissionogenic</sub> ratio of 18.1 ± 2.3 based on Th/U ratios of 4.6 ± 1.6 for the Beacon Sandstone (Balco et al., 2011; G. Balco, personal communication, 2011) and the methodology of Ballentine and Burnard (2002) (Supplementary Table S1). Thus, the total <sup>21</sup>Ne<sub>c</sub> component for each sample was determined as follows:

$$\text{Ne}_{\text{excess}} = \frac{\text{Ne}_{\text{measured}}}{\left[ \left( \frac{\text{Ne}_{\text{measured}}}{\text{Ne}_{\text{air}}} \right)_{\text{measured}} - \left( \frac{\text{Ne}_{\text{measured}}}{\text{Ne}_{\text{air}}} \right)_{\text{air}} \right]} \quad (3)$$

$$\text{Ne}_c = \text{Ne}_{\text{excess}} - \text{Ne}_{\text{nucleogenic}} \quad (4)$$

The CRONUS-A standard was also analyzed and found to have a Ne isotopic composition that is indistinguishable from a two component mixture of atmospheric and cosmogenic Ne (Table S1). A two component deconvolution of CRONUS-A indicates that the concentration of <sup>21</sup>Ne<sub>c</sub> is 330 ± 3 × 10<sup>6</sup> atoms g<sup>-1</sup>, within the range observed by Balco and Shuster (2009) (Supplementary Fig. S4). However, measurements of fissionogenic <sup>136</sup>Xe indicate that 13 ± 2 × 10<sup>6</sup> atoms g<sup>-1</sup> out of the 330 ± 3 × 10<sup>6</sup> atoms g<sup>-1</sup> of excess <sup>21</sup>Ne measured are nucleogenic. Thus, even when the Ne isotopic composition of a sample falls within error of the two-component mixing line, a few percent of the excess <sup>21</sup>Ne may be nucleogenic in origin.

## 3. Results

The measured sample concentrations of cosmogenic <sup>21</sup>Ne<sub>c</sub> and <sup>10</sup>Be along with sampling site information are presented in Table 1. Under the assumption of two component Ne mixing, sample concentrations of excess <sup>21</sup>Ne (Eq. (3)) serve as an upper limit for cosmogenic concentrations of <sup>21</sup>Ne and are generally quite low compared to previous measurements in sandstones

**Table 1**  
Cosmogenic nuclide concentrations and sample site information.

Sample Name	Location	Lat. S	Long. E	Alt. (m)	Z (cm)	f <sub>shield</sub>	α <sup>a</sup> (deg.)	Cosmogenic <sup>21</sup> Ne <sup>b</sup> (10 <sup>6</sup> atoms g <sup>-1</sup> )	Cosmogenic <sup>10</sup> Be (10 <sup>6</sup> atoms g <sup>-1</sup> )	<sup>21</sup> Ne Erosion Rate <sup>c</sup> (cm Ma <sup>-1</sup> )	<sup>10</sup> Be Erosion Rate <sup>c</sup> (cm Ma <sup>-1</sup> )	Average Erosion Rate <sup>d</sup> (cm Ma <sup>-1</sup> )
<i>Battleship Promontory Samples</i>												
BP08-273	Trans Bench	76.9084	160.9410	970	6	1.00	< 15	26.8 ± 2.5	5.13 ± 0.14	124 <sup>+13</sup> <sub>-11</sub> – 183 <sup>+22</sup> <sub>-18</sub>	128 <sup>+5</sup> <sub>-4</sub> – 146 <sup>+6</sup> <sub>-5</sub>	128 ± 4 – 149 ± 5
BP08-215	Trans	76.9084	160.9410	963	6	0.50	< 15	19.4 ± 2.6	3.10 ± 0.11	85 <sup>+13</sup> <sub>-10</sub> – 118 <sup>+22</sup> <sub>-17</sub>	101 <sup>+5</sup> <sub>-4</sub> – 113 <sup>+6</sup> <sub>-5</sub>	99 ± 4 – 113 ± 5
BP08-319	Trans	76.9084	160.9410	960	3	0.50	< 15	12.5 ± 2.5	2.35 ± 0.12	136 <sup>+34</sup> <sub>-23</sub> – 204 <sup>+58</sup> <sub>-39</sub>	146 <sup>+9</sup> <sub>-8</sub> – 169 <sup>+11</sup> <sub>-10</sub>	145 ± 8 – 171 ± 10
<b>BP Trans Average<sup>e</sup></b>								<b>15.7 ± 1.8</b>	<b>2.76 ± 0.08</b>	<b>106<sup>+14</sup><sub>-11</sub> – 153<sup>+24</sup><sub>-19</sub></b>	<b>118<sup>+4</sup><sub>-4</sub> – 134<sup>+5</sup><sub>-5</sub></b>	<b>117 ± 4 – 135 ± 5</b>
<i>Sessrumnir Valley Samples:</i>												
SR08-104	Trans I Bench	77.6098	160.9469	1564	3.5	0.98	< 15	53.0 ± 2.7	9.03 ± 0.26	98 <sup>+5</sup> <sub>-7</sub> – 129 <sup>+8</sup> <sub>-7</sub>	111 <sup>+4</sup> <sub>-4</sub> – 122 <sup>+5</sup> <sub>-5</sub>	106 ± 3 – 124 ± 4
SR08-007	Trans I	77.6098	160.9469	1562	2	0.51	80	18.6 ± 2.5	3.30 ± 0.07	65 <sup>+10</sup> <sub>-10</sub> – 92 <sup>+16</sup> <sub>-12</sub>	77 <sup>+2</sup> <sub>-2</sub> – 87 <sup>+3</sup> <sub>-2</sub>	76 ± 2 – 87 ± 2
SR08-008	Trans I	77.6098	160.9469	1558	5.5	0.51	80	17.4 ± 3.2	3.59 ± 0.16	65 <sup>+15</sup> <sub>-10</sub> – 92 <sup>+23</sup> <sub>-16</sub>	64 <sup>+4</sup> <sub>-3</sub> – 76 <sup>+4</sup> <sub>-4</sub>	64 ± 3 – 73 ± 4
SR08-009	Trans I	77.6098	160.9469	1555	6	0.51	80	11.9 ± 2.6	2.40 ± 0.06	94 <sup>+26</sup> <sub>-17</sub> – 138 <sup>+41</sup> <sub>-26</sub>	101 <sup>+3</sup> <sub>-3</sub> – 118 <sup>+4</sup> <sub>-4</sub>	101 ± 3 – 118 ± 4
SR08-010	Trans I	77.6098	160.9469	1552	5	0.51	80	11.1 ± 2.6	2.22 ± 0.04	102 <sup>+31</sup> <sub>-19</sub> – 150 <sup>+47</sup> <sub>-30</sub>	112 <sup>+2</sup> <sub>-2</sub> – 131 <sup>+3</sup> <sub>-3</sub>	112 ± 2 – 131 ± 3
<b>SR Trans I Average<sup>e</sup></b>								<b>14.5 ± 1.3</b>	<b>2.51 ± 0.03</b>	<b>80<sup>+8</sup><sub>-7</sub> – 114<sup>+13</sup><sub>-11</sub></b>	<b>100<sup>+1</sup><sub>-1</sub> – 115<sup>+2</sup><sub>-2</sub></b>	<b>100 ± 1 – 115 ± 2</b>
SR08-077	Trans II Bench	77.6076	160.9516	1541	2	1.00	< 15	78.6 ± 3.0	11.75 ± 0.34	70 <sup>+3</sup> <sub>-3</sub> – 88 <sup>+4</sup> <sub>-4</sub>	84 <sup>+3</sup> <sub>-3</sub> – 92 <sup>+4</sup> <sub>-4</sub>	77 ± 2 – 90 ± 3
SR08-021	Trans II	77.6076	160.9516	1537	5	0.54	75	26.2 ± 3.6	4.45 ± 0.14	50 <sup>+8</sup> <sub>-6</sub> – 67 <sup>+12</sup> <sub>-9</sub>	58 <sup>+2</sup> <sub>-2</sub> – 64 <sup>+3</sup> <sub>-3</sub>	57 ± 2 – 64 ± 3
SR08-022	Trans II	77.6076	160.9516	1533	2.5	0.54	75	13.3 ± 2.5	3.18 ± 0.06	102 <sup>+24</sup> <sub>-16</sub> – 150 <sup>+37</sup> <sub>-25</sub>	91 <sup>+2</sup> <sub>-2</sub> – 104 <sup>+3</sup> <sub>-2</sub>	91 ± 2 – 104 ± 2
SR08-023	Trans II	77.6076	160.9516	1530	3.5	0.54	< 15	18.8 ± 2.7	3.34 ± 0.13	149 <sup>+16</sup> <sub>-13</sub> – 210 <sup>+25</sup> <sub>-21</sub>	185 <sup>+9</sup> <sub>-8</sub> – 211 <sup>+11</sup> <sub>-10</sub>	176 ± 7 – 211 ± 10
SR08-024	Trans II	77.6076	160.9516	1530	3	0.54	75	12.5 ± 2.5	2.86 ± 0.06	108 <sup>+27</sup> <sub>-18</sub> – 158 <sup>+42</sup> <sub>-28</sub>	101 <sup>+3</sup> <sub>-3</sub> – 117 <sup>+3</sup> <sub>-3</sub>	101 ± 3 – 117 ± 3
SR08-025	Trans II	77.6076	160.9516	1528	6	0.54	75	17.7 ± 2.4	3.79 ± 0.10	72 <sup>+11</sup> <sub>-9</sub> – 102 <sup>+18</sup> <sub>-14</sub>	68 <sup>+2</sup> <sub>-2</sub> – 77 <sup>+3</sup> <sub>-3</sub>	68 ± 2 – 78 ± 3
<b>SR Trans II Average<sup>e</sup></b>								<b>16.7 ± 1.2</b>	<b>3.26 ± 0.04</b>	<b>93<sup>+6</sup><sub>-6</sub> – 133<sup>+10</sup><sub>-10</sub></b>	<b>87<sup>+1</sup><sub>-1</sub> – 100<sup>+2</sup><sub>-2</sub></b>	<b>88 ± 1 – 101 ± 1</b>
RAK96-150B	Bench	77.6146	160.9639	1600	2	0.99	< 15	106 ± 2.9	15.40 ± 0.19	54 <sup>+2</sup> <sub>-1</sub> – 65 <sup>+2</sup> <sub>-2</sub>	61 <sup>+1</sup> <sub>-1</sub> – 66 <sup>+1</sup> <sub>-1</sub>	59 ± 1 – 66 ± 1
RAK96-153	Channel Floor	77.6140	160.9539	1578	2	0.91	< 15	26.1 ± 2.8	4.78 ± 0.06	200 <sup>+19</sup> <sub>-16</sub> – 290 <sup>+29</sup> <sub>-25</sub>	235 <sup>+3</sup> <sub>-3</sub> – 272 <sup>+4</sup> <sub>-4</sub>	234 ± 3 – 272 ± 4
SR08-027	Trans II Floor	77.6076	160.9503	1527	3	0.97	< 15	18.6 ± 2.3	3.69 ± 0.12	283 <sup>+39</sup> <sub>-31</sub> – 420 <sup>+60</sup> <sub>-48</sub>	319 <sup>+12</sup> <sub>-11</sub> – 380 <sup>+16</sup> <sub>-15</sub>	315 ± 11 – 383 ± 15

<sup>a</sup> α indicates sample surface slope angle.

<sup>b</sup> For samples with replicated Ne analyses, concentrations listed here represent the unweighted average concentrations of cosmogenic <sup>21</sup>Ne.

<sup>c</sup> Steady state erosion rates calculated using Stone (2000) scaling following Lal (1991) with attenuation lengths corrections for slope angle following Dunne et al. (1999). The range in rates indicates those calculated assuming the steady state spallation production of <sup>21</sup>Ne<sub>c</sub> and <sup>10</sup>Be (low end, labeled "Sp.") to those determined from the inclusion of 14 Ma of muon production of <sup>21</sup>Ne<sub>c</sub> and <sup>10</sup>Be in addition to steady state spallation production following Balco and Shuster (2009) (high end, labeled "Sp. + mu.".).

<sup>d</sup> Erosion rate calculated from the error weighted average of the rates derived from <sup>21</sup>Ne<sub>c</sub> and <sup>10</sup>Be.

<sup>e</sup> Transect averages represent the <sup>21</sup>Ne<sub>c</sub> and <sup>10</sup>Be error weighted mean for non-bench transect samples, respectively.

from the Dry Valleys (Supplementary Table S2; Balco and Shuster, 2009; Schäfer et al., 1999; Summerfield et al., 1999). The values of  $^{21}\text{Ne}_c$  presented in Table 1, however, have been corrected for nucleogenic Ne following Eq. (4) and are thus even lower. The average concentration and  $1\sigma$  standard deviation of fissionogenic  $^{136}\text{Xe}$  within the subset of samples for which both Ne and Xe were measured were used to estimate a nucleogenic  $^{21}\text{Ne}$  concentration within the Beacon Sandstone of  $7.7 \pm 2.4 \times 10^6 \text{ atoms g}^{-1}$  (Supplementary Table S2). This value was used to calculate  $^{21}\text{Ne}_c$  from the excess  $^{21}\text{Ne}$  concentrations in samples without direct  $^{136}\text{Xe}$  measurements. Due to low concentrations of  $^{21}\text{Ne}_c$ , nucleogenic  $^{21}\text{Ne}$  is a significant component in our samples and represents up to 40% of excess  $^{21}\text{Ne}$ . Similar nucleogenic Ne components may well exist in previously measured Dry Valleys sandstones, but the Ne isotopic ratio would not result in significant deviations from the two component mixing line due to higher relative concentrations of  $^{21}\text{Ne}_c$ .

After correcting for topographic shielding and sample thickness, Sessrummir Valley samples (average elevation 1550 m) range from 20 to  $109 \times 10^6 \text{ atoms g}^{-1}$  of  $^{21}\text{Ne}_c$  and from 3.9 to  $15.8 \times 10^6 \text{ atoms g}^{-1}$  of  $^{10}\text{Be}$ . The Battleship Promontory samples (average elevation 961 m) range from 25 to  $41 \times 10^6 \text{ atoms g}^{-1}$  of  $^{21}\text{Ne}_c$  and from 4.8 to  $6.5 \times 10^6 \text{ atoms g}^{-1}$  of  $^{10}\text{Be}$ . Despite accounting for the relatively large topographic shielding corrections and shorter effective attenuation lengths of the sloped transect samples (Dunne et al., 1999), the cosmogenic nuclide contents of our samples are much lower than that observed in previous analyses of sandstone bedrock within the upland Dry Valleys (Balco and Shuster, 2009; Brown et al., 1991; Nishiizumi et al., 1991; Schäfer et al., 1999; Summerfield et al., 1999). For ease of inter-site comparison of our samples, we plot our cosmogenic data in a  $^{10}\text{Be}/^{21}\text{Ne}-^{21}\text{Ne}$  space in which concentrations of both  $^{21}\text{Ne}_c$  and  $^{10}\text{Be}$  have been normalized to a production rate of 1 by dividing each sample concentration by its altitude specific production rate (e.g., Balco and Shuster (2009); Fig. 4). Ne–Be data from Balco and Shuster (2009), which represent the lower range of cosmogenic nuclide concentrations measured in previous work, are included in Fig. 4 for comparison. In addition, as debate continues on the relative importance of the muon contribution to cosmogenic nuclide production (e.g., Balco and Shuster, 2009; Braucher et al., 2011), we plot a steady state curve for nuclide production through spallation only, as well as a curve corresponding to steady state spallation production with the addition of 14 Ma of muon generated nuclide accumulation at each erosion rate. We choose the 14 Ma time period as this is the age typically associated with the pothole and channel systems of the Dry Valleys (see Section 1). All samples appear consistent with the assumption of steady state erosion over the past several million years (up to 14 Ma).

Propagating errors for nucleogenic  $^{21}\text{Ne}$  derived from Xe analysis leads to relatively large uncertainties in  $^{21}\text{Ne}_c$  for individual samples. In addition, our calculated erosion rates from multiple samples within a single transect do not vary systematically with transect depth. Therefore, we use the error weighted average of the cosmogenic nuclide concentrations from each of the three transects to better constrain representative exposure histories and lateral erosion rates for the three sampling locations (Table 1). These averages are calculated after scaling sample concentrations to similar altitudes, but we note that cosmogenic nuclide production varies by only a few percent within the 15 m span in elevation of each transect and thus potential altitude scaling errors do not affect our conclusions. The bench and channel floor samples reflect the effects of vertical erosion rather than lateral retreat of the pothole walls, thus, these samples were not included in the transect averages.

We present a range of steady state erosion rates derived from  $^{21}\text{Ne}_c$ ,  $^{10}\text{Be}$ , and the error weighted average of the two (Table 1).

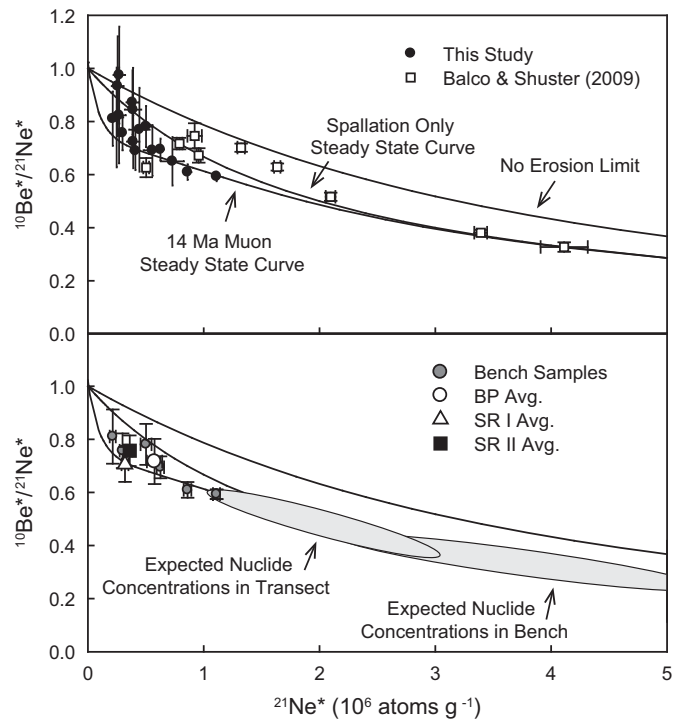


**Fig. 4.**  $^{21}\text{Be}/^{21}\text{Ne}-^{21}\text{Ne}$  plot of normalized cosmogenic nuclide data. The superscripted asterisks in the axes labels indicate that cosmogenic nuclide concentrations for both  $^{21}\text{Ne}$  and  $^{10}\text{Be}$  have been normalized to a production rate of 1 by dividing each concentration by its sample specific production rate, to ease comparison between sampling sites (e.g., Balco and Shuster, 2009). In each plot, the zero erosion limit, the spallation only steady state curve, and the steady state spallation curve with the addition of 14 Ma of muon generated nuclides are shown (Section 3). Upper panel: cosmogenic nuclide contents of sandstone bedrock from previous work in the upland Dry Valleys (Balco and Shuster, 2009) are included for comparison. Lower panel: bench samples are highlighted and  $^{21}\text{Ne}$  error-weighted transect averages are included. Gray ovals indicate expected cosmogenic nuclide concentrations for bench samples and transect samples if exposed for 14 Ma at erosion rates between 10 and  $30 \text{ cm Ma}^{-1}$ .

The low end of the range is the value calculated assuming the production of cosmogenic nuclides only through spallation reactions in steady state, while the high end of the range is the value calculated assuming 14 Ma of muon induced production of nuclides in addition to steady state spallation production. When we compute minimum exposure ages based on our steady state erosion rates, we find that the minimum age of each sample varies by several millions of years based on the inclusion or exclusion of muon induced cosmogenic nuclide production in our erosion rate estimates. Due to the wide range of minimum age estimates, we do not find them meaningful in interpretation of the pothole and channel features and thus do not report them here.

We find that average steady state erosion rates for horizontal wall retreat across the three pothole transects range from 88 to  $135 \text{ cm Ma}^{-1}$ . Vertical down-cutting erosion rates from individual bench samples are more variable and range from 59 to  $149 \text{ cm Ma}^{-1}$ . Vertical erosion rates of the channel floor samples are significantly higher and range from 234 to  $383 \text{ cm Ma}^{-1}$ .

## 4. Discussion

### 4.1. A dearth of cosmogenic nuclides

If the potholes and channels were formed in the mid-Miocene and have experienced continuous exposure at erosion rates

typical of the Dry Valleys ( $10\text{--}30 \text{ cm Ma}^{-1}$ ; Brown et al., 1991; Nishiizumi et al., 1991; Schäfer et al., 1999; Summerfield et al., 1999), then these features would have only widened and deepened by  $1.4\text{--}4.2 \text{ m}$  during the past  $14 \text{ Ma}$ , i.e., the present day length scale of the potholes and channels would be a relic of the landscape at  $14 \text{ Ma}$ . However,  $14 \text{ Ma}$  of exposure at the slow erosion rates within this range would produce cosmogenic nuclide concentrations ranging  $210\text{--}532 \times 10^6 \text{ atoms g}^{-1}$  of  $^{21}\text{Ne}_c$  and  $24\text{--}35 \times 10^6 \text{ atoms g}^{-1}$  of  $^{10}\text{Be}$  in the bench surfaces and  $49\text{--}131 \times 10^6 \text{ atoms g}^{-1}$  of  $^{21}\text{Ne}_c$  and  $7.3\text{--}13 \times 10^6 \text{ atoms g}^{-1}$  of  $^{10}\text{Be}$  in the pothole and channel walls,  $\sim 3\text{--}9$  times higher than those measured in our samples (Fig. 4). Thus, both the  $^{21}\text{Ne}_c$  and  $^{10}\text{Be}$  levels of our samples are surprisingly low compared to that expected given the assumed age of the potholes and the typical erosion rates measured elsewhere in the Dry Valleys.

Small scale topographic shielding effects such as from pits and overhangs along pothole transects may have differed in the past, such that modern shielding estimates overestimate the long-term cosmogenic nuclide production rates at our sampling locations. Yet, such a scenario demands that all of the sampled sites which presently project outward from the pothole and channel walls be shielded in cavities blocking over 80% of incoming cosmic rays during the past  $14 \text{ Ma}$ . Such dramatic shielding would require each sampling location to be, on average, beneath a rock slope overhanging at a  $45^\circ$  angle, a proposition that seems highly unlikely. Moreover, we note that most of the flat bench and channel floor samples, which would not have experienced significant small scale topographic shielding through time, also reveal cosmogenic nuclide concentrations far too low to have experienced a  $14 \text{ Ma}$  duration of exposure at an erosion rate between  $10$  and  $30 \text{ cm Ma}^{-1}$  (Fig. 4).

The average transect erosion rates of  $88\text{--}135 \text{ cm Ma}^{-1}$  determined in this study (Table 1) would cause  $12\text{--}19 \text{ m}$  of lateral retreat along pothole and channel walls while transect bench vertical erosion rates of  $59\text{--}149 \text{ cm Ma}^{-1}$  would carve a channel or pothole  $8\text{--}21 \text{ m}$  deep over the course of  $14 \text{ Ma}$ , similar to the length scales of the present pothole and channel systems. The implied amount of bedrock removed at these relatively high erosion rates over long time scales suggests that significant amounts, or even all, of the material carved out of the pothole and channel systems could have been removed subaerially. Hence, the low  $^{21}\text{Ne}_c$  and  $^{10}\text{Be}$  concentrations of our samples suggest that the channel systems are eroding much faster than previously assumed and, either the pothole surfaces formed primarily through subaerial mechanisms, or the surfaces have experienced complex exposure histories since the mid-Miocene.

#### 4.2. Channel and pothole formation through subaerial erosive processes

The simplest interpretation of the lower cosmogenic nuclide concentrations in this study compared to previous analyses from the region is that the pothole and channel systems have experienced higher erosion rates than other parts of the Dry Valleys (Balco and Shuster, 2009; Brown et al., 1991; Ivy-Ochs et al., 1995; Margerison et al., 2005; Nishiizumi et al., 1991; Schäfer et al., 1999; Summerfield et al., 1999). This explanation is consistent with the deeply weathered appearance of the pothole and channel systems, including rock fall debris. Additionally, it may not be surprising for the unique morphology of the pothole and channel systems to reflect higher and more variable erosion rates than the surrounding regions within the Dry Valleys. In other words, it may be reasonable to find higher erosion rates within regions in which large amounts of bedrock have obviously been removed, such as the pothole and channel systems.

The relatively high steady state erosion rates calculated for both wall retreat and vertical down-cutting in the pothole and

channel systems indicate that the subaerial erosion processes within the upland Dry Valleys, be they driven by liquid water or by other means, can be locally powerful enough to carve these features over the course of millions of years without the influence of subglacial mechanisms (Section 4.1). Alternatively, the pothole and channel systems might have been initiated subglacially at  $14 \text{ Ma}$  and then continuously eroded at the rates determined here, suggesting that the length scale of these features has been greatly amplified by subaerial mechanisms since the mid-Miocene. Thus, the high flow volume of subglacial flooding inferred to be required to carve these features based on observations of the modern morphology (Denton and Sugden, 2005) would be an overestimate of the flow experienced at  $14 \text{ Ma}$ . In either case, the presence of these pothole and channels systems does not necessitate catastrophic subglacial flooding and we emphasize that subaerial preservation of these geomorphic features since the mid-Miocene is inconsistent with the cosmogenic nuclide data.

#### 4.3. Miocene age for the channel systems requires a complex exposure history

If the pothole and channel morphology observed today does indeed record mid-Miocene subglacial processes, then a complex exposure history is required to limit the amount of erosion experienced by these features over the past  $14 \text{ Ma}$  and prevent the accumulation of cosmogenic nuclide concentrations above those observed in our samples. Complex exposure histories generate cosmogenic nuclide signatures that are fit by multiple solutions. We propose below two possible mechanisms to explain the cosmogenic signature of our data under the assumption that the potholes and channels were formed in the mid-Miocene ( $14 \text{ Ma}$ ).

##### 4.3.1. A dramatic increase in Plio–Pleistocene erosion rates

The potholes and channels could have been continuously exposed since a mid-Miocene formation at the low erosion rates typical elsewhere in the Dry Valleys if they have experienced dramatically higher erosion rates within the past few million years. A threefold increase in erosion rates would rapidly remove the top nuclide-rich layers of bedrock within the pothole and channel systems and thus expose the nuclide-poor surface beneath. The surface would establish a new steady state at the higher erosion rate within a few million years. For example, an exposure history for a model surface experiencing  $11 \text{ Ma}$  of continuous exposure at an erosion rate of  $30 \text{ cm Ma}^{-1}$ , followed by  $3 \text{ Ma}$  of exposure at an increased erosion rate of  $100 \text{ cm Ma}^{-1}$  generates  $^{21}\text{Ne}_c$  and  $^{10}\text{Be}$  concentrations within the range of our data (Fig. 5). However, the environmental changes required to cause such a jump in erosion rates within the last few million years are not readily apparent. Further, we note that such an exposure history would still remove enough material to carve over a third of the pothole and channel depths, significantly modifying the morphology of these features. Again, if a subglacial flood origin is assumed for the pothole and channel features based on modern length scale observations, then major amplification of the pothole and channel sizes after their initial formation suggests that flood flow volume estimates derived from the hypothesis of negligible erosion are too high.

##### 4.3.2. Prolonged ice cover

Alternatively, extensive shielding by a single or multiple episodes of cover could prevent severe erosion or the accumulation of high levels of cosmogenic nuclides over the past  $14 \text{ Ma}$ . For example,  $4.5 \text{ m}$  of ice cover on a horizontal surface decreases the spallation production of new nuclides by 95%, but does not affect the loss of radionuclides through radioactive decay. The loss of  $^{10}\text{Be}$  relative to  $^{21}\text{Ne}_c$  during periods of cover generates a complex

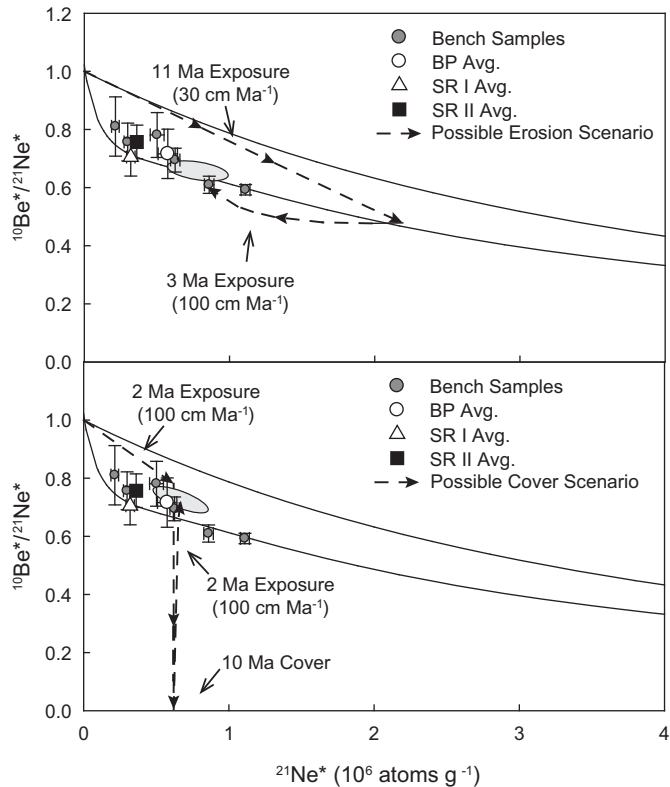


**Fig. 5.** Examples of complex exposure histories that generate cosmogenic nuclide concentrations within the range of our transect averages. Gray ovals demonstrate the range of nuclide concentrations generated for both flat bench samples and sloped surfaces up to 80°. The superscripted asterisks in the axes labels indicate that the concentrations in the diagram have been normalized to a production rate of 1 as in Fig. 4. Both panels include the steady state curve that includes 14 Ma of muon interactions in addition to the steady state spallation production of both nuclides. Upper panel: dashed line illustrates the evolution of the cosmogenic signature as a model surface experiences 11 Ma of exposure at an erosion rate of  $30 \text{ cm Ma}^{-1}$  followed by 3 Ma of exposure at an erosion rate of  $100 \text{ cm Ma}^{-1}$ . Lower panel: the evolution of the cosmogenic signature as a model surface experiences an initial 2 Ma of exposure at an erosion rate of  $100 \text{ cm Ma}^{-1}$ , followed by 10 Ma of ice cover, and a subsequent 2 Ma of exposure at the same erosion rate.

signature on the cosmogenic  $^{10}\text{Be}/^{21}\text{Ne}_c - ^{21}\text{Ne}$  plot. However, at all erosion rates, the complex signature of ice cover is lost within 2 Ma of subsequent exposure as the uncovered surfaces reestablish steady state with respect to  $^{10}\text{Be}$ . Importantly, the steady state erosion rates calculated for our samples assume a simple exposure history (Table 1; Section 4.1) and would not be applicable if the samples have been covered.

Measurements of cosmogenic  $^{26}\text{Al}$  and  $^{10}\text{Be}$  from a sandstone landslide deposit in Arena Valley (Putkonen et al., 2008), as well as from higher elevation samples collected within the northern valleys of the Western Asgard Range (Nishiizumi et al., 1991), plot on the steady state line, suggesting no cover within the past 2 Ma. If the same recent exposure history is applicable to Battleship Promontory and Sessrummir Valley, then any cover that preserved Miocene morphology must have disappeared by 2 Ma. Given these constraints, an exposure history consisting of 2 Ma of exposure, 10 Ma of cover, and 2 Ma of additional exposure also fits our data. The most recent 2 Ma of subaerial exposure provide a lower limit on the erosion rates of our most cosmogenic nuclide-rich sample of  $55 \text{ cm Ma}^{-1}$ , though an erosion rate of  $100 \text{ cm Ma}^{-1}$  better fits our transect average data (Fig. 5). Surfaces eroding at a rate slower than  $55 \text{ cm Ma}^{-1}$  would accumulate higher levels of  $^{21}\text{Ne}_c$  than those measured in our samples over 4 Ma of total exposure. Miocene age surfaces experiencing

durations of cover shorter than 10 Ma would require higher erosion rates to stay within the range of cosmogenic nuclide concentrations in our samples.

Sandy sediments are a possible cover material within Battleship Promontory and Sessrummir Valley. Windblown sand and snow drifts are observed currently shielding lower sections of channel walls within some areas in Battleship Promontory and Sessrummir Valley, but not around the sampling locations. The source of the volume of sediment required to fill the pothole and channel systems and cover the benches above the potholes, however, is not apparent and would imply extreme geomorphic changes and dramatic movement of material within the upland Dry Valleys since the mid-Miocene.

A more plausible cover material is cold-based ice. Previous work has concluded that the Western Asgard Range has remained ice free since  $\sim 13.5$  Ma based on the apparent lack of typical moraine or drift evidence recording more recent alpine glaciations (Denton et al., 1993). However, the cold-based alpine glaciers of Antarctica often do not produce conspicuous geologic traces. The most obvious marks of cold-based glaciers, boulder belt moraines, are relatively rare finds as they require debris input to the ice surface and favorable geometry to form. For example, most of the current small cold-based alpine glaciers to the south of the Western Asgard Range do not have such moraines. Additionally, although previous cosmogenic  $^{10}\text{Be}$  and  $^{26}\text{Al}$  data in the Dry Valleys do not indicate ice cover within the last 2 Ma, they cannot be used to rule out the possibility of prolonged periods of alpine glaciations during the Miocene and Pliocene.

Cold-based alpine glaciers currently cover all but the highest ridges of the Eastern Asgard Range, only 15 km to the east of Sessrummir Valley (Fig. 6). During past episodes of decreased sea ice extent and open waters in McMurdo Sound (Naish et al., 2009), precipitation may have increased in the western Dry Valleys. Increased inland snowfall could lead to the formation of analogous cold-based glaciers in Battleship Promontory and Sessrummir Valley. The recent work of Swanger et al. (2011) concludes that the Taylor Glacier reached a highstand in the Pliocene  $\sim 200$  m higher than present day in Kennar Valley,  $\sim 20$  km southwest of Sessrummir Valley (Fig. 1). An increase of 200 m in glacial thickness would fill the south facing valleys of the Western Asgard Range and would be nearly sufficient to overtop the passes along the divide. A thicker Taylor Glacier would lower the topographic barrier of the Asgard Range and may have led to an increase in windblown snow accumulation on the northern side of the mountains and into the uplands of the Western Asgard Range. Analogous increases in ice volume surrounding the Convoy Range and a subsequent increased accumulation of windblown snow could have supported the presence of cold-based glaciers there as well during the Pliocene. However, if our sampled surfaces are the remnants of Miocene age morphology, then any mechanism called upon for the production of cold-based glaciers in Battleship Promontory and Sessrummir Valley must be applicable in the Miocene as well as the Pliocene. Otherwise, the combination of  $10\text{--}30 \text{ cm Ma}^{-1}$  erosion rates and 3 Ma of glacial ice cover during the Pliocene would not adequately limit the buildup of  $^{21}\text{Ne}_c$  and  $^{10}\text{Be}$  to the low levels observed in our samples. In other words, if the potholes and channels were formed in the Miocene and if proposed conditions conducive to the generation of cold-based glaciers are unique to the Pliocene, then glacial ice cover by itself cannot fully explain the low cosmogenic nuclide concentration of our samples.

## 5. Conclusion

Our observations refute the dual hypotheses that the pothole and channel systems of Battleship Promontory and Sessrummir

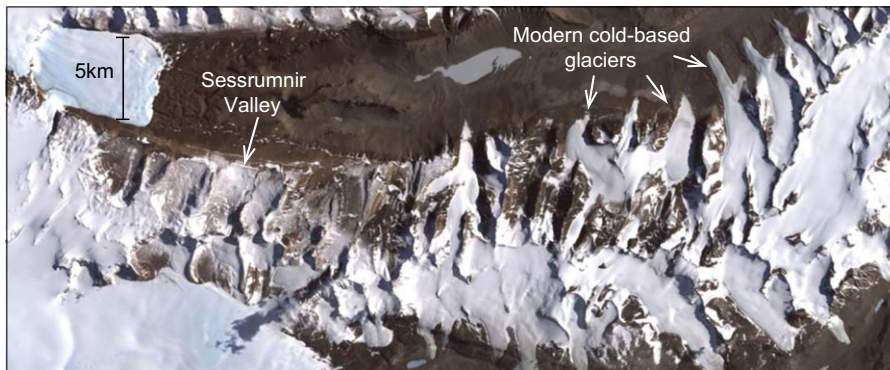


**Fig. 6.** Cold-based alpine glaciers cover all but the ridges in the eastern Asgard Range ~15 km from Sessrumnir Valley. We hypothesize that during periods of decreased sea ice extent in McMurdo Sound, precipitation may have increased in the more inland western Dry Valleys, forming alpine glaciers in regions like Sessrumnir Valley. We note that a small glacier currently occupies the head of Sessrumnir Valley ~3 km from the channel systems. Landsat imagery courtesy of NASA Goddard Space Flight Center and U.S. Geological Survey.

Valley were formed subglacially in the mid-Miocene and have been continuously exposed at low erosion rates for the past 14 Ma. Steady state erosion rates determined from cosmogenic  $^{21}\text{Ne}$  and  $^{10}\text{Be}$  concentrations suggest that the entirety of the pothole and channel systems could have been excavated sub-aerially since the mid-Miocene and thus the formation of these features does not require catastrophic subglacial flooding under a massive EAIS. Alternatively, if these features were largely formed subglacially in the Miocene, then they must have experienced large increases in erosion rates prior to 2 Ma or nearly 10 Ma of cover throughout the time interval since their formation. The mechanism capable of increasing erosion rates threefold within the past few million years is, however, not apparent. On the other hand, the proximity of low-erosive cold-based glaciers to our field sites and documented fluctuations of the adjacent EAIS outlet glaciers are consistent with the possibility that episodes of cover could be caused by cold-based ice. Irrespective of whether the pothole and channel systems have lost tens of meters of bedrock over the past 14 Ma, have experienced a factor of three increase in Plio-Pleistocene erosion rates, or have been covered by significant episodes of ice since the Miocene, the landscape of the Dry Valleys' uplands is likely more dynamic than previously thought.

## Acknowledgments

The project was supported by U.S. National Science Foundation grant number ANT-0739452. We thank Raytheon Polar Services and the Air National Guard for logistical support, Robert McBrearty and Allen Pope for assistance during field work in the Dry Valleys, and Greg Balco for providing Th/U data on the Beacon Sandstone. Samuel Niedermann and an anonymous reviewer are also thanked for providing comments helpful for the improvement of the manuscript.

## Appendix A. Supporting information

Supplementary data associated with this article can be found in the online version at <http://dx.doi.org/10.1016/j.epsl.2012.08.017>.

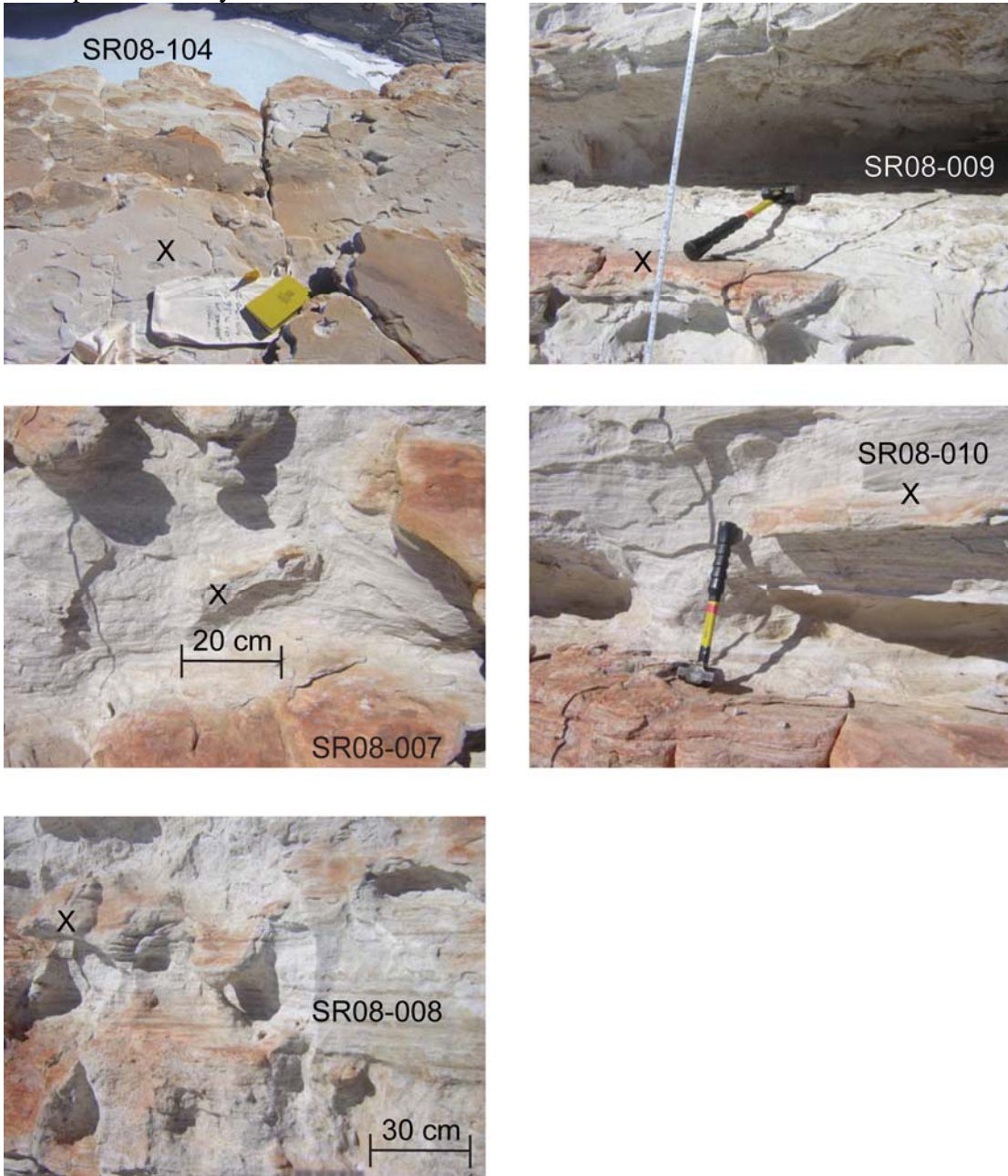
## References

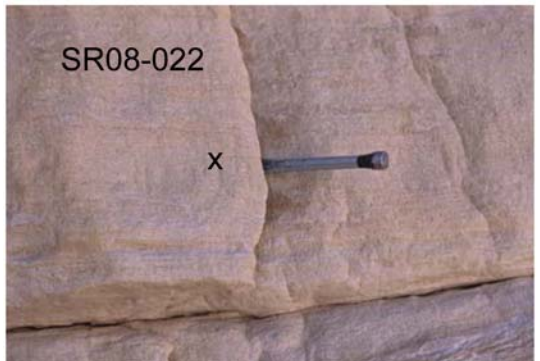
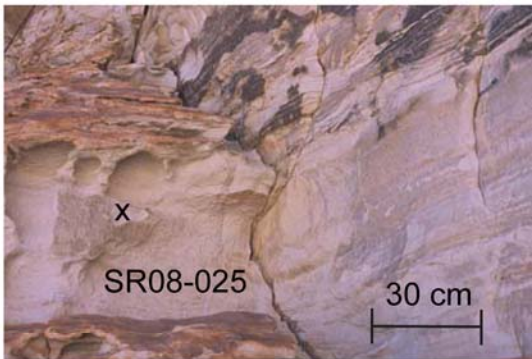
- Balco, G., Shuster, D.L., 2009. Production rate of cosmogenic  $^{21}\text{Ne}$  in quartz estimated from  $^{10}\text{Be}$ ,  $^{26}\text{Al}$ , and  $^{21}\text{Ne}$  concentrations in slowly eroding Antarctic bedrock surfaces. *Earth Planet. Sci. Lett.* 281, 48–58.
- Balco, G., Shuster, D.L., Blard, P.-H., Zimmermann, L., Stone, J.O.H., 2011. Cosmogenic  $^{21}\text{Ne}$  production systematics in quartz inferred from a 25-meter sandstone core. *Mineral. Mag.* 75, 473.
- Ballentine, C.J., Burnard, P.G., 2002. Production, release, and transport of noble gases in the continental crust. *Rev. Mineral. Geochem.* 47, 481–538.
- Benito, G., O'Connor, J.E., 2003. Number and size of last-glacial Missoula floods in the Columbia River valley between the Pasco Basin, Washington, and Portland Oregon. *Geol. Soc. Am. Bull.* 115, 624–638.
- Braucher, R., Merchel, S., Borgoman, J., Bourlès, D.L., 2011. Production of cosmogenic radionuclides at great depth: a multielement approach. *Earth Planet. Sci. Lett.* 309, 1–9.
- Bretz, J.H., 1969. Lake Missoula floods and channeled scabland. *J. Geol.* 77, 505–543.
- Brown, E., Edmond, T.J., Raisbeck, G.M., Yiou, F., Kurz, M.D., Brook, E.J., 1991. Examination of surface exposure ages of Antarctic moraines using in-situ produced  $^{10}\text{Be}$  and  $^{26}\text{Al}$ . *Geochim. Cosmochim. Acta* 55, 2269–2283.
- Denton, G.H., Sugden, D.E., 2005. Meltwater features that suggest Miocene ice sheet overriding of the Transantarctic Mountains in Victoria Land, Antarctica. *Geogr. Ann.* 87A, 67–85.
- Denton, G.H., Prentice, M.L., Kellogg, D.E., Kellogg, T.B., 1984. Late Tertiary history of the Antarctic Ice-Sheet – evidence from the Dry Valleys. *Geology* 12, 263–267.
- Denton, G.H., Sugden, D.E., Marchant, D., Hall, B., Wilch, T., 1993. East Antarctic ice sheet sensitivity to Pliocene climatic change from a Dry Valleys perspective. *Geogr. Ann.* 75A, 155–204.
- Dowsett, H., Barron, J., Poore, R., 1996. Middle Pliocene sea surface temperatures: a global reconstruction. *Mar. Micropaleontol.* 27, 13–25.
- Dunne, J., Elmore, D., Muzikar, P., 1999. Scaling factors for the rates of production of cosmogenic nuclides for geometric shielding and attenuation at depth on sloped surfaces. *Geomorphology* 27, 3–11.
- Fujioka, T., Chappell, J., Honda, M., Yatsevich, I., Fifield, K., Fabel, D., 2005. Global cooling initiated stony deserts in central Australia 2–4 Ma dated by cosmogenic  $^{21}\text{Ne}$ – $^{10}\text{Be}$ . *Geology* 33, 993–996.
- Goehring, B.M., 2006.  $^{10}\text{Be}$  Exposure Ages of Erratic Boulders in Southern Norway and Implications for the History of the Fennoscandian Ice Sheet, M.S. thesis, Oregon State University.
- Goethals, M.M., Hetzel, R., Niedermann, S., Wittman, H., Fenton, C.R., Kubik, P.W., Christl, M., von Blanckenburg, F., 2009. An improved experimental determination of cosmogenic  $^{10}\text{Be}$ / $^{21}\text{Ne}$  and  $^{26}\text{Al}$ / $^{21}\text{Ne}$  production ratios in quartz.
- Gosse, J.C., Phillips, F.M., 2001. Terrestrial in situ cosmogenic nuclides: theory and application. *Q. Sci. Rev.* 20, 1475–1560.
- Heisinger, B., Lal, D., Jull, A.J.T., Kubik, P., Ivy-Ochs, S., Neumaier, S., Knie, K., Lazarev, V., Nolte, E., 2002a. Production of selected cosmogenic radionuclides by muons 1. Fast muons. *Earth Planet. Sci. Lett.* 200, 345–355.
- Heisinger, B., Lal, D., Jull, A.J.T., Kubik, P., Ivy-Ochs, S., Knie, K., Nolte, E., 2002b. Production of selected cosmogenic radionuclides by muons: 2. Capture of negative muons. *Earth Planet. Sci. Lett.* 200, 357–369.
- Ivy-Ochs, S., Schlüchter, C., Kubik, P.W., Dittrich-Hannen, B., Beer, J., 1995. Minimum  $^{10}\text{Be}$  exposure ages of early Pliocene for the Table Mountain plateau and the Sirius Group at Mt. Fleming, Dry Valleys, Antarctica. *Geology* 23, 1007–1010.
- Korschinek, G., Bergmaier, A., Faestermann, T., Geerstmann, U.C., Knie, K., Rugel, G., Wallner, A., Dillmann, I., Dollinger, G., Lierse von Gostomoski, Ch., Kosssert, K., Maiti, M., Poutivstev, M., Remmert, A., 2010. A new value for the half-life of  $^{10}\text{Be}$  by heavy-ion elastic recoil detection and liquid scintillation counting. *Nucl. Instrum. Methods Phys. Res. B* 268, 187–191.
- Lal, D., 1991. Cosmic-ray labeling of erosion surfaces – in situ nuclide production rates and erosion models. *Earth Planet. Sci. Lett.* 104, 424–439.

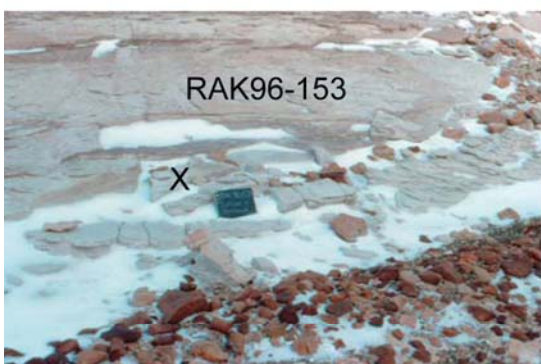
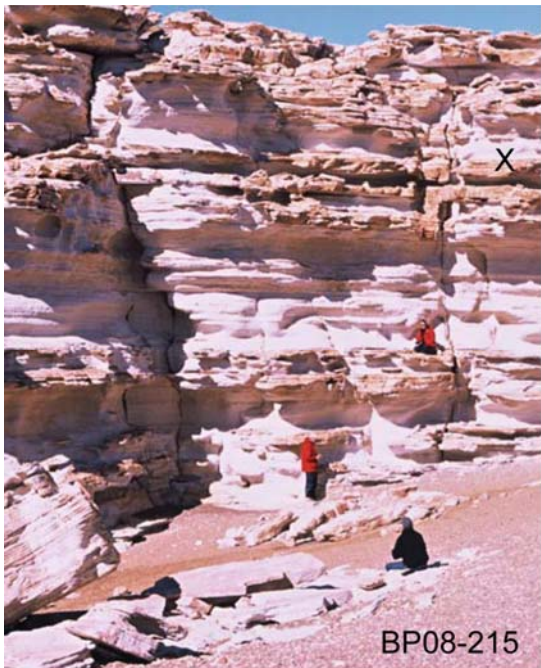
- Lewis, A.R., Marchant, D.R., Kowalewski, D.E., Baldwin, S.L., Webb, L.E., 2006. The age and origin of the Labyrinth, western Dry Valleys, Antarctica: evidence for extensive middle Miocene subglacial floods and freshwater discharge to the Southern Ocean. *Geology* 34, 513–516.
- Licciardi, J.F., 2000. Alpine Glacier and Pluvial Lake Records of Late Pleistocene Climate Variability in the Western United States, Ph.D. thesis, Oregon State University.
- Marchant, D.R., Denton, G.H., 1996. Miocene and Pliocene paleoclimate of the Dry Valleys region, Southern Victoria land: a geomorphological approach. *Mar. Micropaleontol.* 27, 253–271.
- Marchant, D.R., Denton, G.H., Sugden, D.E., Swisher, C.C., 1993a. Miocene glacial stratigraphy and landscape evolution of the Western Asgard Range. *Geogr. Ann.* 75A, 303–330.
- Marchant, D.R., Swisher, C.C., Lux, D.R., West, D.P., Denton, G.H., 1993b. Pliocene Paleoclimate and East Antarctic ice-sheet history from surficial ash deposits. *Science* 260, 667–670.
- Margerison, H.R., Phillips, W.M., Stuart, F.M., Sugden, D.E., 2005. Cosmogenic  $^3\text{He}$  concentrations in ancient flood deposits from the Coombs Hills, northern Dry Valleys, East Antarctica: interpreting exposure ages and erosion rates. *Earth Planet. Sci. Lett.* 230, 163–175.
- Naish, T., Powell, R., Levy, R., Wilson, G., Scherer, R., Talarico, F., Krissek, L., Niessen, F., Pompilio, M., Wilson, T., Carter, L., DeConto, R., Huybers, P., McKay, R., Pollard, D., Ross, J., Winter, D., Barnett, P., Browne, G., Cody, R., Cowan, E., Crampton, J., Dunbar, G., Dunbar, N., Florindo, F., Gebhardt, C., Graham, I., Hannah, M., Hansraj, D., Harwood, D., Helling, D., Henrys, S., Hinnow, L., Kuhn, G., Kyle, P., Läufer, A., Maffioli, P., Magens, D., Mandernack, K., McIntosh, W., Millan, C., Morin, R., Ohneiser, C., Paulsen, T., Persico, D., Raine, I., Reed, J., Riesselman, C., Sagnotti, L., Schmitt, D., Sjunneskog, C., Strong, P., Taviani, M., Vogel, S., Wilch, T., Williams, T., 2009. Obliquity-paced Pliocene West Antarctic ice sheet oscillations. *Nature* 458, 322–329.
- Niedermann, S., 2002. Cosmic-ray-produced noble gases in terrestrial rocks: dating tools for surface processes. *Rev. Mineral. Geochem.* 47, 731–784.
- Nishiizumi, K., Imamura, M., Caffee, M.W., Southon, J.R., Finkel, R.C., McAninch, J., 2007. Absolute calibration of  $^{10}\text{Be}$  AMS standards. *Nucl. Instrum. Methods Phys. Res. B* 258, 403–413.
- Nishiizumi, K., Kohl, C.P., Arnold, J.R., Klein, J., Fink, D., Middleton, R., 1991. Cosmic ray produced  $^{10}\text{Be}$  and  $^{26}\text{Al}$  in Antarctic rocks: exposure and erosion history. *Earth Planet. Sci. Lett.* 104, 440–454.
- Putkonen, J., Balco, G., Morgan, D., 2008. Slow regolith degradation without creep determined by cosmogenic nuclide measurements in Arena Valley, Antarctica. *Q. Res.* 69, 242–249.
- Ravelo, A.C., Andreassen, D.H., Lyle, M., Lyle, A.O., Wara, M.W., 2004. Regional climate shifts caused by gradual global cooling in the Pliocene epoch. *Nature* 429, 263–267.
- Schäfer, J.M., Ivy-Ochs, S., Wieler, R., Leya, I., Baur, H., Denton, G.H., Schlüchter, C., 1999. Cosmogenic noble gas studies in the oldest landscape on earth: surface exposure ages of the Dry Valleys, Antarctica. *Earth Planet. Sci. Lett.* 167, 215–226.
- Shaw, J., Healy, T.R., 1977. Formation of Labyrinth, Wright Valley, Antarctica. *N. Z. J. Geol. Geophys.* 20, 933–947.
- Selby, M.J., Wilson, A.T., 1971. The origin of the Labyrinth, Wright Valley, Antarctica. *Geol. Soc. Am. Bull.* 82, 471–476.
- Stone, J.O., 2000. Air pressure and cosmogenic isotope production. *J. Geophys. Res.* 105 (B10), 23753–23759.
- Sugden, D.E., Denton, G.H., 2004. Cenozoic landscape evolution of the Convoy Range to Mackay Glacier area, Transantarctic Mountains: onshore to offshore synthesis. *Geol. Soc. Am. Bull.* 116, 840–857.
- Sugden, D.E., Denton, G.H., Marchant, D.R., 1991. Subglacial meltwater channel systems and ice sheet overriding, Asgard Range, Antarctica. *Geogr. Ann.* 73A, 109–121.
- Summerfield, M., Stuart, F., Cockburn, H., Sugden, D., Denton, G., Dunai, T., Marchant, D., 1999. Long-term rates of denudation in the Dry Valleys, Transantarctic Mountains, southern Victoria Land, Antarctica based on in-situ-produced cosmogenic  $^{21}\text{Ne}$ . *Geomorphology* 27, 113–129.
- Swanger, K.M., Marchant, D.R., Schäfer, J.M., Winckler, G., Head, J.W., 2011. Elevated East Antarctic outlet glaciers during warmer-than-present climates in southern Victoria Land. *Global Planet. Change* 79, 61–72.

## Supplementary Materials:

**Fig. S1.** Below are close up field photographs of all 17 samples presented in our study. Each panel is labeled with the appropriate sample name. X's mark sample location. SR and RAK samples are from the Sessrumnir Valley channel systems, BP samples are from a single pothole in Battleship Promontory.







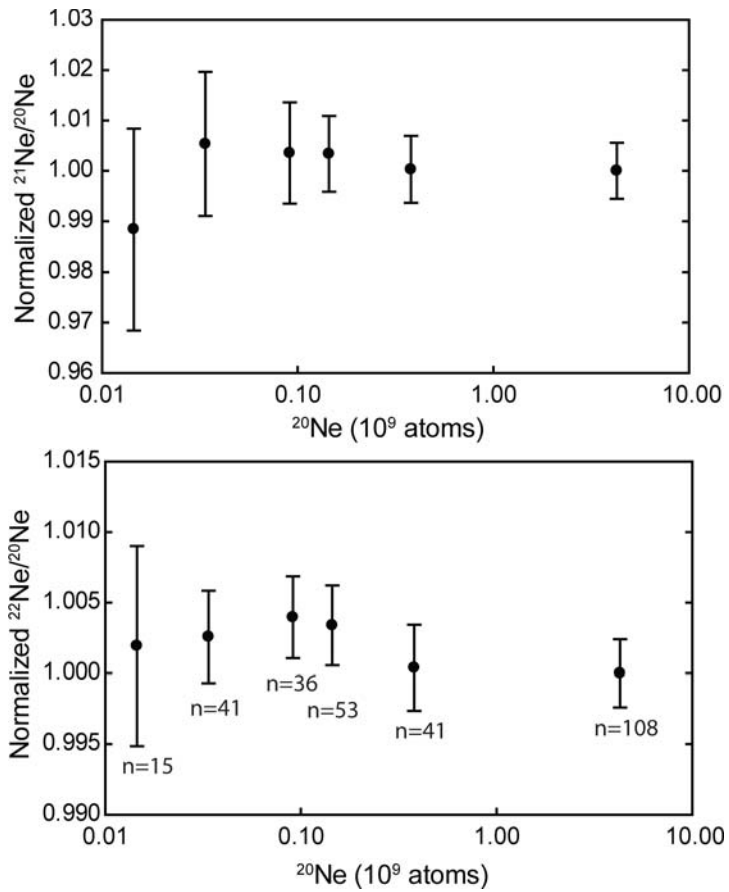


**Fig. S2.** Mass discrimination of the  $^{21}\text{Ne}/^{20}\text{Ne}$  and  $^{22}\text{Ne}/^{20}\text{Ne}$  ratios as a function of the Ne signal. The  $^{21}\text{Ne}/^{20}\text{Ne}$  and  $^{22}\text{Ne}/^{20}\text{Ne}$  ratios for the different sized standards were normalized to the  $^{21}\text{Ne}/^{20}\text{Ne}$  and  $^{22}\text{Ne}/^{20}\text{Ne}$  ratios of the largest standard ( $4.3 \times 10^9$  atoms of  $^{20}\text{Ne}$ ), respectively. The errors reflect the relative uncertainties in the  $^{21}\text{Ne}/^{20}\text{Ne}$  and  $^{22}\text{Ne}/^{20}\text{Ne}$  ratios based on the reproducibility of the standards run over a five month period.

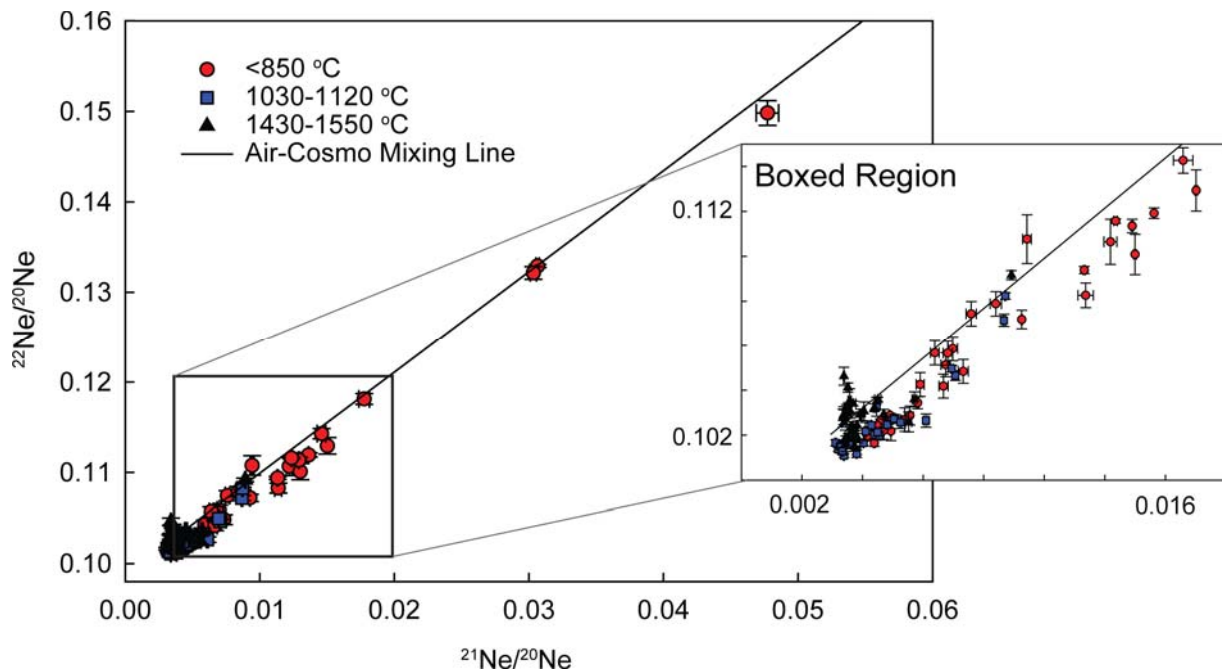


**Fig. S3.** Neon isotope plot normalized to  $^{20}\text{Ne}$  for evolved sample Ne at the low temperature, middle temperature, and high temperature heat steps. The solid line represents the two component mixing line between air sourced neon with a  $^{21}\text{Ne}/^{20}\text{Ne}$  ratio of  $0.002959 \pm 0.00004$  and a  $^{22}\text{Ne}/^{20}\text{Ne}$  ratio of  $0.102 \pm 0.0008$  (Porcelli et al., 2002) and purely cosmogenic sourced neon in quartz with a  $^{21}\text{Ne}/^{20}\text{Ne}$  ratio of  $0.8 \pm 0.1$  and a  $^{22}\text{Ne}/^{20}\text{Ne}$  ratio of  $0.993 \pm 0.14$  (Niedermann, 2002). Samples in this study contain a significant nucleogenic  $^{21}\text{Ne}$  component in addition to  $^{21}\text{Ne}$  from air and cosmogenic sources.

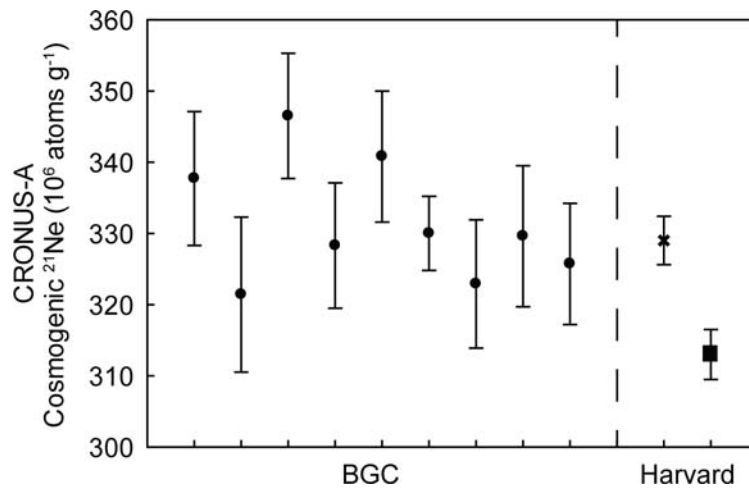


**Fig. S4.** A comparison of analyses of cosmogenic  $^{21}\text{Ne}$  in the CRONUS-A standard between Berkeley Geochronology Center (BGC) (Balco and Shuster, 2009) and the Noble Gas Laboratory at Harvard (this study). The X indicates the CRONUS-A concentration determined using the assumption that released  $^{21}\text{Ne}$  is a two component mixture of air and a cosmogenic source. The square indicates the CRONUS-A concentration determined by correcting for nucleogenic  $^{21}\text{Ne}$  from measurement of fissionogenic  $^{136}\text{Xe}$ .

**Table S1:** Neon measurements and isotope ratios from step heating of samples. ‘J’ and ‘M’ labeled samples are replicate measurements on quartz that was chemically purified for the  $^{10}\text{Be}$  measurements.

Sample Name	Temp <sup>a</sup> °C	$^{20}\text{Ne}$ ( $10^9$ atoms g $^{-1}$ )	$^{21}\text{Ne}/^{20}\text{Ne}$ (ratio x 10 $^{-3}$ )	$^{22}\text{Ne}/^{20}\text{Ne}$ (ratio x 10 $^{-3}$ )	Excess $^{21}\text{Ne}$ (10 $^6$ atoms g $^{-1}$ )
BP08-273	750	$0.5996 \pm 0.0050$	11.37 $\pm$ 0.26	108.08 $\pm$ 0.65	$5.06 \pm 0.16$
	1120	$5.54 \pm 0.12$	7.065 $\pm$ 0.062	104.67 $\pm$ 0.63	$22.87 \pm 0.60$
	1550	$3.31 \pm 0.06$	5.713 $\pm$ 0.076	103.54 $\pm$ 0.62	$9.14 \pm 0.30$
BP08-273-J	530	$1.403 \pm 0.023$	13.054 $\pm$ 0.046	112.77 $\pm$ 0.30	$14.16 \pm 0.24$
	1030	$15.45 \pm 0.14$	4.036 $\pm$ 0.012	101.53 $\pm$ 0.11	$16.19 \pm 0.24$
	1550	$1.736 \pm 0.028$	3.682 $\pm$ 0.041	102.23 $\pm$ 0.28	$1.255 \pm 0.075$
BP08-215	750	$1.953 \pm 0.016$	5.90 $\pm$ 0.13	104.07 $\pm$ 0.63	$5.78 \pm 0.26$
	1120	$17.74 \pm 0.29$	3.805 $\pm$ 0.030	101.32 $\pm$ 0.61	$15.08 \pm 0.59$
	1530	$8.04 \pm 0.2$	3.734 $\pm$ 0.032	101.52 $\pm$ 0.61	$6.25 \pm 0.29$
BP08-319	750	$0.6422 \pm 0.0054$	6.67 $\pm$ 0.15	104.00 $\pm$ 0.63	$2.39 \pm 0.10$
	1120	$3.641 \pm 0.068$	6.100 $\pm$ 0.072	102.61 $\pm$ 0.62	$11.48 \pm 0.34$
	1550	$2.352 \pm 0.028$	5.52 $\pm$ 0.10	102.46 $\pm$ 0.62	$6.05 \pm 0.25$
BP08-319-J	410	$0.5425 \pm 0.0091$	12.18 $\pm$ 0.21	110.65 $\pm$ 1.0	$5.00 \pm 0.14$
	590	$2.484 \pm 0.039$	4.938 $\pm$ 0.024	102.18 $\pm$ 0.43	$4.92 \pm 0.10$
	1030	$20.69 \pm 0.20$	3.389 $\pm$ 0.016	101.083 $\pm$ 0.067	$8.89 \pm 0.35$
	1550	$3.305 \pm 0.052$	3.425 $\pm$ 0.024	101.83 $\pm$ 0.39	$1.539 \pm 0.083$
SR08-104	750	$1.668 \pm 0.015$	14.59 $\pm$ 0.32	114.08 $\pm$ 0.69	$19.46 \pm 0.56$
	1120	$16.98 \pm 0.14$	4.974 $\pm$ 0.023	102.68 $\pm$ 0.62	$34.38 \pm 0.48$
	1550	$13.76 \pm 0.13$	3.606 $\pm$ 0.017	102.34 $\pm$ 0.62	$8.93 \pm 0.25$
SR08-104-J	410	$0.5428 \pm 0.0092$	47.73 $\pm$ 0.84	149.83 $\pm$ 1.4	$24.30 \pm 0.61$
	590	$3.014 \pm 0.048$	9.252 $\pm$ 0.024	107.18 $\pm$ 0.41	$18.97 \pm 0.31$
	1030	$21.84 \pm 0.20$	3.599 $\pm$ 0.014	101.585 $\pm$ 0.076	$13.97 \pm 0.32$
	1550	$3.384 \pm 0.053$	3.350 $\pm$ 0.024	102.76 $\pm$ 0.40	$1.321 \pm 0.084$
SR08-007-J	410	$0.833 \pm 0.014$	15.012 $\pm$ 0.050	112.93 $\pm$ 0.92	$10.04 \pm 0.17$
	590	$2.827 \pm 0.045$	5.563 $\pm$ 0.024	102.87 $\pm$ 0.42	$7.36 \pm 0.13$
	1030	$23.77 \pm 0.22$	3.270 $\pm$ 0.020	101.353 $\pm$ 0.052	$7.40 \pm 0.49$
	1550	$3.570 \pm 0.056$	3.374 $\pm$ 0.024	102.87 $\pm$ 0.39	$1.481 \pm 0.089$
SR08-008	750	$1.418 \pm 0.012$	6.74 $\pm$ 0.15	104.94 $\pm$ 0.63	$5.39 \pm 0.22$
	1120	$11.88 \pm 0.32$	4.098 $\pm$ 0.043	102.16 $\pm$ 0.62	$13.58 \pm 0.62$
	1550	$6.58 \pm 0.14$	3.574 $\pm$ 0.057	103.44 $\pm$ 0.62	$4.05 \pm 0.38$
SR08-008-M*	750	$17.80 \pm 0.15$	4.157 $\pm$ 0.021	101.93 $\pm$ 0.10	$21.40 \pm 0.41$
	1120	$16.69 \pm 0.14$	3.199 $\pm$ 0.016	101.37 $\pm$ 0.10	$4.01 \pm 0.27$
	1550	$3.979 \pm 0.035$	3.464 $\pm$ 0.080	103.25 $\pm$ 0.10	$2.01 \pm 0.32$
SR08-009-J	410	$0.747 \pm 0.012$	13.997 $\pm$ 0.049	110.09 $\pm$ 0.90	$7.50 \pm 0.13$
	590	$2.982 \pm 0.047$	4.700 $\pm$ 0.024	102.21 $\pm$ 0.40	$5.19 \pm 0.11$
	1030	$23.38 \pm 0.22$	3.200 $\pm$ 0.027	101.495 $\pm$ 0.029	$5.63 \pm 0.63$
	1550	$2.851 \pm 0.045$	3.386 $\pm$ 0.024	104.62 $\pm$ 0.40	$1.218 \pm 0.071$

Table S1, continued.

Sample Name	Temp <sup>a</sup> °C	<sup>20</sup> Ne (10 <sup>9</sup> atoms g <sup>-1</sup> )	<sup>21</sup> Ne/ <sup>20</sup> Ne (ratio x 10 <sup>-3</sup> )	<sup>22</sup> Ne/ <sup>20</sup> Ne (ratio x 10 <sup>-3</sup> )	Excess <sup>21</sup> Ne (10 <sup>6</sup> atoms g <sup>-1</sup> )
SR08-010	750	1.308 ± 0.012	5.39 ± 0.12	102.50 ± 0.62	3.19 ± 0.16
	1120	11.43 ± 0.10	3.807 ± 0.021	101.18 ± 0.61	9.72 ± 0.26
	1550	7.57 ± 0.13	3.526 ± 0.031	101.91 ± 0.61	4.31 ± 0.24
SR08-010-J*	750	11.71 ± 0.22	4.388 ± 0.030	101.65 ± 0.15	16.80 ± 0.48
	1120	14.66 ± 0.21	3.111 ± 0.026	101.66 ± 0.13	2.23 ± 0.39
	1550	1.72 ± 0.03	3.385 ± 0.057	102.92 ± 0.22	0.74 ± 0.10
SR08-077	750	1.667 ± 0.014	17.76 ± 0.40	117.92 ± 0.71	24.77 ± 0.69
	1120	12.32 ± 0.20	6.948 ± 0.042	104.98 ± 0.63	49.36 ± 0.79
	1550	9.50 ± 0.16	4.391 ± 0.035	103.24 ± 0.62	13.67 ± 0.40
SR08-077-J*	750	9.51 ± 0.24	11.321 ± 0.030	109.39 ± 0.16	79.9 ± 2.0
	1120	19.42 ± 0.20	3.392 ± 0.021	101.52 ± 0.12	8.43 ± 0.41
	1550	2.101 ± 0.041	3.517 ± 0.049	104.12 ± 0.21	1.18 ± 0.11
SR08-021	750	1.544 ± 0.013	6.98 ± 0.16	105.66 ± 0.64	6.23 ± 0.25
	1120	11.25 ± 0.17	4.819 ± 0.038	102.47 ± 0.62	20.99 ± 0.53
	1550	7.33 ± 0.16	3.946 ± 0.040	102.90 ± 0.62	7.25 ± 0.33
SR08-021-M*	750	14.88 ± 0.12	4.751 ± 0.024	102.67 ± 0.10	26.77 ± 0.41
	1120	16.38 ± 0.14	3.355 ± 0.017	101.64 ± 0.10	6.51 ± 0.28
	1550	4.530 ± 0.039	3.690 ± 0.085	103.41 ± 0.10	3.32 ± 0.39
SR08-022	750	1.503 ± 0.013	6.81 ± 0.15	105.47 ± 0.64	5.82 ± 0.24
	1120	8.80 ± 0.16	4.388 ± 0.038	102.03 ± 0.61	12.64 ± 0.41
	1550	6.01 ± 0.13	3.722 ± 0.034	101.98 ± 0.61	4.60 ± 0.22
SR08-022-J	410	0.692 ± 0.012	13.161 ± 0.020	112.38 ± 0.33	7.06 ± 0.18
	590	1.995 ± 0.032	5.818 ± 0.039	103.48 ± 0.27	5.70 ± 0.12
	1030	12.84 ± 0.12	3.342 ± 0.015	101.20 ± 0.16	4.91 ± 0.20
	1550	1.482 ± 0.024	3.640 ± 0.046	104.45 ± 0.30	0.942 ± 0.070
SR08-023	750	1.591 ± 0.013	7.32 ± 0.16	104.45 ± 0.63	6.97 ± 0.27
	1120	8.48 ± 0.17	4.557 ± 0.043	101.99 ± 0.61	13.61 ± 0.46
	1550	5.88 ± 0.13	3.840 ± 0.034	101.88 ± 0.61	5.19 ± 0.23
SR08-023-M*	750	11.360 ± 0.095	4.589 ± 0.023	102.63 ± 0.10	18.58 ± 0.30
	1120	14.29 ± 0.12	3.284 ± 0.016	101.53 ± 0.10	4.66 ± 0.24
	1550	3.343 ± 0.030	3.530 ± 0.081	102.95 ± 0.10	1.91 ± 0.27
SR08-024	750	1.113 ± 0.009	6.39 ± 0.14	105.48 ± 0.64	3.83 ± 0.16
	1120	7.95 ± 0.13	4.497 ± 0.040	102.13 ± 0.62	12.27 ± 0.38
	1550	5.73 ± 0.13	3.67 ± 0.04	102.32 ± 0.62	4.07 ± 0.23
SR08-025	750	1.0355 ± 0.0093	7.59 ± 0.17	107.25 ± 0.65	4.81 ± 0.18
	1120	7.32 ± 0.14	5.047 ± 0.047	102.74 ± 0.62	15.36 ± 0.46
	1550	5.73 ± 0.12	3.823 ± 0.035	102.44 ± 0.62	4.97 ± 0.23

Table S1, continued.

Sample Name	Temp <sup>a</sup> °C	<sup>20</sup> Ne (10 <sup>9</sup> atoms g <sup>-1</sup> )	<sup>21</sup> Ne/ <sup>20</sup> Ne (ratio x 10 <sup>-3</sup> )	<sup>22</sup> Ne/ <sup>20</sup> Ne (ratio x 10 <sup>-3</sup> )	Excess <sup>21</sup> Ne (10 <sup>6</sup> atoms g <sup>-1</sup> )
SR08-025-J*	750	12.49 ± 0.24	4.779 ± 0.031	102.66 ± 0.15	22.82 ± 0.58
	1120	12.56 ± 0.24	3.157 ± 0.031	101.49 ± 0.15	2.49 ± 0.39
	1550	1.47 ± 0.03	3.515 ± 0.059	104.23 ± 0.22	0.817 ± 0.088
SR08-027	750	1.166 ± 0.010	8.40 ± 0.19	107.68 ± 0.65	6.37 ± 0.23
	1120	6.04 ± 0.14	5.253 ± 0.053	102.57 ± 0.62	13.91 ± 0.45
	1550	4.86 ± 0.13	4.049 ± 0.042	103.06 ± 0.62	5.31 ± 0.25
SR08-027M*	750	13.14 ± 0.11	4.475 ± 0.022	102.44 ± 0.10	20.00 ± 0.34
	1120	14.57 ± 0.12	3.288 ± 0.016	101.48 ± 0.10	4.80 ± 0.24
	1550	3.509 ± 0.031	3.499 ± 0.081	103.06 ± 0.10	1.90 ± 0.28
RAK96-150B	850	1.776 ± 0.015	30.33 ± 0.23	132.14 ± 0.80	48.78 ± 0.58
	1030	6.51 ± 0.10	8.667 ± 0.053	107.15 ± 0.65	37.29 ± 0.66
	1430	12.01 ± 0.26	4.701 ± 0.028	102.93 ± 0.62	21.00 ± 0.56
RAK96-150B-M*	750	8.614 ± 0.072	12.354 ± 0.061	111.57 ± 0.11	81.23 ± 0.86
	1120	18.14 ± 0.15	4.289 ± 0.021	102.44 ± 0.10	24.22 ± 0.43
	1550	9.980 ± 0.084	3.920 ± 0.019	102.94 ± 0.10	9.63 ± 0.21
RAK96-153	850	1.826 ± 0.015	9.43 ± 0.14	110.77 ± 0.67	11.86 ± 0.28
	1030	7.67 ± 0.17	4.463 ± 0.055	103.27 ± 0.62	11.58 ± 0.50
	1430	13.14 ± 0.27	3.448 ± 0.042	101.62 ± 0.61	6.44 ± 0.57
RAK96-153-M*	750	11.61 ± 0.10	4.904 ± 0.024	102.88 ± 0.10	22.66 ± 0.34
	1120	17.95 ± 0.15	3.338 ± 0.017	101.30 ± 0.10	6.83 ± 0.30
	1550	8.193 ± 0.069	3.389 ± 0.078	102.55 ± 0.10	3.54 ± 0.64
CRONUS-A*	750	10.595 ± 0.090	30.76 ± 0.12	132.91 ± 0.17	295.6 ± 2.8
	1120	4.576 ± 0.072	8.752 ± 0.028	108.24 ± 0.14	26.62 ± 0.44
	1550	1.154 ± 0.026	8.865 ± 0.046	109.17 ± 0.20	6.84 ± 0.16

\*Xe measurements were also carried out on these samples during step heating (Table S2).

<sup>a</sup>Reported temperatures are based on a calibration between pyrometer readings of the furnace hot spot, where samples are baked, and thermocouple readings taken at each heat step (Section 2.2). Pyrometer readings of 750°C, 1120°C, and 1550°C, correspond with thermocouple readings of 700°C, 900°C, and 1250°C, respectively.

**Table S2:** Xenon analyses for estimating the nucleogenic component ( $^{21}\text{Ne}_{\text{nuc}}$ ) of observed  $^{21}\text{Ne}$  from fissionogenic  $^{136}\text{Xe}$  ( $^{136}\text{Xe}_{\text{fiss}}$ ). Sample names are as listed in Table S1.

Sample Name	Temp <sup>a</sup> (°C)	$^{129}\text{Xe}$ ( $10^6$ atoms g <sup>-1</sup> )	$^{129}\text{Xe}/^{130}\text{Xe}$	$^{136}\text{Xe}/^{129}\text{Xe}$	$^{136}\text{Xe}_{\text{fiss}}$ ( $10^6$ atoms g <sup>-1</sup> )	$^{21}\text{Ne}_{\text{nuc}}$ ( $10^6$ atoms g <sup>-1</sup> )
SR08-008-M	750	7.40 ± 0.11	6.51 ± 0.05	0.3667 ± 0.0045	0.235 ± 0.034	
	1120	2.992 ± 0.043	6.51 ± 0.10	0.3605 ± 0.0044	0.077 ± 0.013	
	1550	31.40 ± 0.45	6.51 ± 0.03	0.3393 ± 0.0042	0.13 ± 0.13	
				<b>Total</b>	<b>0.45 ± 0.18</b>	<b>8.1 ± 3.5</b>
SR08-10-J	750	11.39 ± 0.35	6.54 ± 0.05	0.3423 ± 0.0036	0.128 ± 0.052	
	1120	3.25 ± 0.10	6.43 ± 0.12	0.3484 ± 0.0080	0.056 ± 0.025	
	1550	10.48 ± 0.33	6.39 ± 0.05	0.3537 ± 0.0038	0.166 ± 0.050	
				<b>Total</b>	<b>0.35 ± 0.13</b>	<b>6.3 ± 2.4</b>
SR08-021-M	750	7.62 ± 0.11	6.40 ± 0.05	0.3807 ± 0.0047	0.349 ± 0.036	
	1120	5.018 ± 0.072	6.55 ± 0.07	0.3481 ± 0.0043	0.066 ± 0.022	
	1550	37.76 ± 0.54	6.45 ± 0.03	0.3400 ± 0.0042	0.191 ± 0.16	
				<b>Total</b>	<b>0.61 ± 0.22</b>	<b>10.9 ± 4.3</b>
SR08-023-M	750	NA*	-	-	-	-
	1120	4.245 ± 0.061	6.50 ± 0.10	0.3595 ± 0.0044	0.104 ± 0.019	
	1550	29.48 ± 0.42	6.48 ± 0.03	0.3419 ± 0.0042	0.204 ± 0.12	
				<b>Total</b>	<b>0.31 ± 0.14</b>	<b>5.6 ± 2.7</b>
SR08-25-J	750	10.78 ± 0.33	6.46 ± 0.05	0.3460 ± 0.0037	0.117 ± 0.050	
	1120	1.923 ± 0.059	6.53 ± 0.10	0.3571 ± 0.0097	0.054 ± 0.015	
	1550	9.21 ± 0.28	6.49 ± 0.06	0.3611 ± 0.0039	0.229 ± 0.037	
				<b>Total</b>	<b>0.40 ± 0.10</b>	<b>7.2 ± 2.1</b>
SR08-027-M	750	13.8 ± 0.20	6.52 ± 0.05	0.3606 ± 0.0044	0.353 ± 0.061	
	1120	4.510 ± 0.065	6.58 ± 0.10	0.3486 ± 0.0043	0.061 ± 0.019	
	1550	49.11 ± 0.71	6.55 ± 0.03	0.3348 ± 0.0041	0	-
				<b>Total</b>	<b>0.41 ± 0.28</b>	<b>7.5 ± 5.4</b>

Table S2, continued.

Sample Name	Temp <sup>a</sup> (°C)	<sup>129</sup> Xe (10 <sup>6</sup> atoms g <sup>-1</sup> )	<sup>129</sup> Xe/ <sup>130</sup> Xe	<sup>136</sup> Xe/ <sup>129</sup> Xe	<sup>136</sup> Xe <sub>fiss</sub> (10 <sup>6</sup> atoms g <sup>-1</sup> )	<sup>21</sup> Ne <sub>nuc</sub> (10 <sup>6</sup> atoms g <sup>-1</sup> )
SR08-77-J	750	10.01 ± 0.20	6.52 ± 0.05	0.3467 ± 0.0038	0.137 ± 0.046	
	1120	1.911 ± 0.038	6.53 ± 0.15	0.405 ± 0.011	0.138 ± 0.022	
	1550	7.12 ± 0.14	6.48 ± 0.06	0.3778 ± 0.0047	0.295 ± 0.034	
				<b>Total</b>	<b>0.57 ± 0.10</b>	<b>10.3 ± 2.3</b>
RAK96-150B-M	750	7.55 ± 0.11	6.50 ± 0.05	0.3462 ± 0.0043	0.084 ± 0.032	
	1120	3.455 ± 0.050	6.48 ± 0.10	0.3490 ± 0.0043	0.048 ± 0.015	
	1550	19.78 ± 0.29	6.49 ± 0.04	0.3378 ± 0.0042	0.055 ± 0.082	
				<b>Total</b>	<b>0.19 ± 0.13</b>	<b>3.4 ± 2.4</b>
RAK96-153-M	750	NA*	-	-	-	-
	1120	4.268 ± 0.061	6.53 ± 0.10	0.3444 ± 0.0042	0.040 ± 0.018	
	1550	28.83 ± 0.42	6.47 ± 0.03	0.3394 ± 0.0042	0.128 ± 0.12	
				<b>Total</b>	<b>0.17 ± 0.14</b>	<b>3.0 ± 2.5</b>
CRONUS-A	750	8.91 ± 0.25	6.48 ± 0.05	0.3801 ± 0.0029	0.386 ± 0.023	
	1120	3.73 ± 0.11	6.46 ± 0.05	0.3661 ± 0.0040	0.105 ± 0.018	
	1550	6.67 ± 0.20	6.46 ± 0.05	0.3765 ± 0.0029	0.258 ± 0.019	
				<b>Total</b>	<b>0.75 ± 0.06</b>	<b>13.5 ± 2.1</b>

\*Xe data could not be collected during the 750°C heat step for these samples. As complete Xe data are not available for these samples, they are corrected for nucleogenic <sup>21</sup>Ne using the average for the Beacon Sandstones.

<sup>a</sup>Reported temperatures are based on a calibration between pyrometer readings of the furnace hot spot, where samples are baked, and thermocouple readings taken at each heat step (Section 2.2). Pyrometer readings of 750°C, 1120°C, and 1550°C, correspond with thermocouple readings of 700°C, 900°C, and 1250°C, respectively.

**References:**

- Balco, G., Shuster, D.L., 2009. Production rate of cosmogenic Ne-21 in quartz estimated from Be-10, Al-26, and Ne-21 concentrations in slowly eroding Antarctic bedrock surfaces. *Earth Planet. Sci. Lett.* 281, 48-58.
- Niedermann, S., 2002. Cosmic-ray-produced noble gases in terrestrial rocks: Dating tools for surface processes. *Rev. Mineral. Geochem.* 47, 731-784.
- Porcelli, D., Ballentine, C.J., Wieler, R., 2002. An overview of noble gas - Geochemistry and cosmochemistry. *Rev. Mineral. Geochem.* 47, 1-19.